The Astrophysical Journal, 942:88 (18pp), 2023 January 10 https://doi.org/10.3847/1538-4357/aca527

Kilonovae and Optical Afterglows from Binary Neutron Star Mergers. II. Optimal Search Strategy for Serendipitous Observations and Target-of-opportunity Observations of Gravitational Wave Triggers

Jin-Ping Zhu[1], Shichao Wu[2,3], Yuan-Pei Yang[4], Chang Liu[1,5], Bing Zhang[6,7], Hao-Ran Song[8], He Gao[8], Zhoujian Cao[8], Yun-Wei Yu[9], Yacheng Kang[1,5], and Lijing Shao[5,10]
[1] Department of Astronomy, School of Physics, Peking University, Beijing 100871, People's Republic of China; zhujp@pku.edu.cn
[2] Max-Planck-Institut für Gravitationsphysik (Albert-Einstein-Institut), D-30167 Hannover, Germany; shichao.wu@aei.mpg.de
[3] Leibniz Universität Hannover, D-30167 Hannover, Germany
[4] South-Western Institute for Astronomy Research, Yunnan University, Kunming, Yunnan, People's Republic of China; ypyang@ynu.edu.cn
[5] Kavli Institute for Astronomy and Astrophysics, Peking University, Beijing 100871, People's Republic of China
[6] Nevada Center for Astrophysics, University of Nevada, Las Vegas, NV 89154, USA; bing.zhang@unlv.edu
[7] Department of Physics and Astronomy, University of Nevada, Las Vegas, NV 89154, USA
[8] Department of Astronomy, Beijing Normal University, Beijing 100875, People's Republic of China
[9] Institute of Astrophysics, Central China Normal University, Wuhan 430079, People's Republic of China
[10] National Astronomical Observatories, Chinese Academy of Sciences, Beijing 100012, People's Republic of China
Received 2022 August 29; revised 2022 November 7; accepted 2022 November 21; published 2023 January 16

Abstract

In the second work of this series, we explore the optimal search strategy for serendipitous and gravitational-wave-triggered target-of-opportunity (ToO) observations of kilonovae and optical short-duration gamma-ray burst (sGRB) afterglows from binary neutron star (BNS) mergers, assuming that cosmological kilonovae are AT2017gfo-like (but with viewing-angle dependence) and that the properties of afterglows are consistent with those of cosmological sGRB afterglows. A one-day cadence serendipitous search strategy with an exposure time of ∼30 s can always achieve an optimal search strategy of kilonovae and afterglows for various survey projects. We show that the optimal detection rates of the kilonovae (afterglows) are $\sim 0.3/0.6/1/20\,\mathrm{yr}^{-1}$ ($\sim 50/60/100/800\,\mathrm{yr}^{-1}$) for Zwicky the Transient Facility (ZTF)/Multi-channel Photometric Survey Telescope (Mephisto)/Wide Field Survey Telescope (WFST)/Large Synoptic Survey Telescope (LSST), respectively. A better search strategy for SiTian than the current design is to increase the exposure time. In principle, a fully built SiTian can detect $\sim 7(2000)\,\mathrm{yr}^{-1}$ kilonovae (afterglows). Population properties of electromagnetic (EM) signals detected by serendipitous observations are studied in detail. For ToO observations, we predict that one can detect $\sim 11\,\mathrm{yr}^{-1}$ BNS gravitational wave (GW) events during the fourth observing run (O4) by considering an exact duty cycle of the third observing run. The median GW sky localization area is expected to be $\sim 10\,\mathrm{deg}^2$ for detectable BNS GW events. For O4, we predict that ZTF/Mephisto/WFST/LSST can detect ∼5/4/3/3 kilonovae (∼1/1/1/1 afterglows) per year, respectively. The GW detection rates, GW population properties, GW sky localizations, and optimistic ToO detection rates of detectable EM counterparts for BNS GW events at the Advanced Plus, LIGO Voyager, and ET&CE eras are detailedly simulated in this paper.

Unified Astronomy Thesaurus concepts: Gravitational waves (678); Neutron stars (1108); Gamma-ray bursts (629)

1. Introduction

Kilonovae (Li & Paczyński 1998; Metzger et al. 2010) and short-duration gamma-ray bursts (sGRB; Paczynski 1986, 1991; Eichler et al. 1989; Narayan et al. 1992; Zhang 2018) have long been thought to originate from binary neutron star (BNS) and neutron star–black hole (NSBH) mergers. The interaction of the sGRB relativistic jets with the surrounding interstellar medium would produce bright afterglow emissions from X-ray to radio[11] (Rees & Meszaros 1992; Mészáros & Rees 1993, 1997; Paczynski & Rhoads 1993; Sari et al. 1998; Gao et al. 2013b).

On 2017 August 17, the first BNS gravitational wave (GW) event, i.e., GW170817, was detected by the Advanced Laser Interferometer Gravitational Wave Observatory (LIGO; Harry & LIGO Scientific Collaboration 2010; LIGO Scientific Collaboration et al. 2015) and the Advanced Virgo (Acernese et al. 2015) detectors (Abbott et al. 2017a). This BNS GW event has been subsequently confirmed in connection with an sGRB (GRB170817A; Abbott et al. 2017b; Goldstein et al. 2017; Savchenko et al. 2017; Zhang et al. 2018), an ultraviolet–optical–infrared kilonova (AT2017gfo; Abbott et al. 2017c; Andreoni et al. 2017; Arcavi et al. 2017; Chornock et al. 2017; Coulter et al. 2017; Covino et al. 2017; Cowperthwaite et al. 2017; Díaz et al. 2017; Drout et al. 2017; Evans et al. 2017; Hu et al. 2017; Kasliwal et al. 2017; Kilpatrick et al. 2017; Lipunov et al. 2017; McCully et al. 2017; Nicholl et al. 2017; Pian et al. 2017; Shappee et al. 2017; Smartt et al. 2017; Soares-Santos et al. 2017; Tanvir et al. 2017; Utsumi et al. 2017; Valenti et al. 2017; Villar et al. 2017), and a broadband off-axis jet afterglow (Alexander et al. 2017; Haggard et al. 2017; Hallinan et al. 2017; Margutti et al. 2017; Troja et al. 2017, 2018, 2020; D'Avanzo et al. 2018; Dobie et al. 2018; Lazzati et al. 2018; Lyman et al. 2018; Xie et al. 2018; Ghirlanda et al. 2019; Piro et al. 2019). The multimessenger

[11] If BNS and NSBH mergers occur in the accretion disks of active galactic nuclei (e.g., Cheng & Wang 1999; McKernan et al. 2020), sGRB relativistic jets would always be choked and kilonova emissions would be outshone by the disk emission (Perna et al. 2021; Zhu et al. 2021e). The choked jets and subsequent jet cocoon and ejecta shock breakouts can generate high-energy neutrinos, which may significantly contribute to diffuse neutrino background (Zhu et al. 2021a, 2021b).

observations of this BNS merger provided smoking-gun evidence for the long-hypothesized origin of sGRBs and kilonovae, and heralded the advent of the GW-led astronomy era.

To date, except for AT2017gfo, other kilonova candidates were all detected in superposition with decaying sGRB afterglows (e.g., Berger et al. 2013; Fan et al. 2013; Tanvir et al. 2013; Gao et al. 2015, 2017; Jin et al. 2015, 2016, 2020; Yang et al. 2015; Gompertz et al. 2018; Ascenzi et al. 2019; Rossi et al. 2020; Fong et al. 2021; Ma et al. 2021; Wu et al. 2021; Yuan et al. 2021). Interestingly, a bright kilonova candidate was recently found to be associated with a long-duration GRB 211211A (e.g., Rastinejad et al. 2022; Troja et al. 2022; Yang et al. 2022b; Zhu et al. 2022a). One possible reason why almost all kilonova candidates were detected in GRB afterglows is that most BNS and NSBH mergers are far away from us. Their associated kilonova signals may be too faint to be directly detected by present survey projects. However, thanks to the beaming effect of relativistic jets, in Paper I of this series (Zhu et al. 2022c), we have shown that a large fraction of cosmological afterglows could be much brighter than the associated kilonovae if the jets move toward or close to the line of sight. Bright afterglow emissions would help us detect potential associated kilonova emissions. On the other hand, a too bright afterglow would also affect the detectability of the associated kilonova.

Catching more kilonovae and afterglows by current and future survey projects would be helpful for expanding our knowledge of the population properties of these events. Kasliwal et al. (2020) and Mohite et al. (2022) constrained the population properties of kilonovae based on the nondetection of GW-triggered follow-up observations during O3. Although the properties of kilonova and afterglow emissions from BNS and NSBH mergers can be reasonably well predicted, their low luminosities and fast evolution nature compared with supernova emission make it difficult to detect them using the traditional time-domain survey projects. Several works in the literature have studied the detection rates and search strategy for kilonovae by serendipitous observations (e.g., Metzger & Berger 2012; Coughlin et al. 2017, 2020b; Rosswog et al. 2017; Scolnic et al. 2018; Setzer et al. 2019; Almualla et al. 2021; Andreoni et al. 2022; Chase et al. 2022; Sagués Carracedo et al. 2021; Zhu et al. 2021e). Because afterglow emission could significantly affect the observation of a fraction of kilonova events, one cannot ignore the effect of afterglow emission when considering the search strategy and detectability of kilonova emission. In the second work of this series, we will perform a detailed study on optimizing serendipitous detections of both kilonovae and optical afterglows with different cadences, filters, and exposure times for several present and future survey projects. The survey projects we consider in this work include the Zwicky Transient Facility (ZTF; Bellm et al. 2019; Masci et al. 2019), the Multi-channel Photometric Survey Telescope[12] (Mephisto; X.-Z. Er et al. 2023, in preparation), the Wide Field Survey Telescope (WFST; X. Kong et al. 2023, in preparation), the Large Synoptic Survey Telescope (LSST; LSST Science Collaboration et al. 2009), and the SiTian Projects (SiTian; Liu et al. 2021). We note that (1) NSBH mergers may have a lower event rate density; (2) NSBH kilonovae may be dimmer than BNS kilonovae (e.g., Zhu et al. 2020); (3) most NSBH mergers in the universe are likely plunging events (e.g., Zappa et al. 2019; Drozda et al. 2022; Abbott et al. 2021a; Broekgaarden et al. 2021; Zhu et al. 2021c, 2022b; Hu et al. 2022). As a result, the detection rates of kilonova and afterglow emissions from NSBH mergers should be much lower than those from BNS mergers (Zhu et al. 2021d). In the following calculations, we only consider sGRB, kilonova, and afterglow emissions from BNS mergers.

Furthermore, with the upgrade and iteration of GW observatories, numerous BNS mergers from the distant universe will be discovered. Future foreseeable GW observations will give a better constraint on the localization for a fraction of BNS GW events, which will benefit the search for associated electromagnetic (EM) counterparts. For example, some GW sources will be localized to $\sim$10 deg^2 by the network including the Advanced LIGO, Advanced Virgo, and Kamioka Gravitational Wave Detector (KAGRA) GW detectors (Abbott et al. 2020a; Frostig et al. 2022). Therefore, taking advantage of target-of-opportunity (ToO) follow-up observations of GW triggers will greatly improve the search efficiency of kilonovae and afterglows, although Petrov et al. (2022) recently suggested that the previous expectations for the GW sky localization may be too optimistic. The kilonova follow-up campaigns by specific survey projects, e.g., ZTF, LSST, and the Wide-Field Infrared Transient Explorer, for GW BNS mergers in the near GW era have been recently simulated (Cowperthwaite et al. 2019; Frostig et al. 2022; Sagués Carracedo et al. 2021). In this paper, we present detailed calculations of the BNS detectability by the GW detectors in the next 15 yr and the associated EM detectability for GW-triggered ToO observations.

The paper is organized as follows. The physical models are briefly presented in Section 2. More details of our models have been presented in Paper I. The search strategy and detectability of kilonova and afterglow emissions for time-domain survey observations are studied in Section 3. We also perform some calculations for the EM detection rates by some specific survey projects. In Section 4, we simulate the GW detection and subsequent detectability of EM ToO follow-up observations for networks of second-, 2.5th-, and third-generation GW detectors. Finally, we summarize our conclusions and present some discussions in Section 5. A standard ΛCDM cosmology with $H_0 = 67.8\,\mathrm{km\,s^{-1}\,Mpc^{-1}}$, $\Omega_\Lambda = 0.692$, and $\Omega_\mathrm{m} = 0.308$ (Planck Collaboration et al. 2016) is applied in this paper.

2. Modeling

2.1. Redshift Distribution and EM Properties of Simulated BNS Populations

The total number of BNS mergers in the universe can be estimated as (e.g., Sun et al. 2015)

$$\dot{N}_\mathrm{BNS} \approx \int_0^{z_\mathrm{max}} \frac{\dot{\rho}_{0,\mathrm{BNS}} f(z)}{1+z} \frac{dV(z)}{dz} dz, \quad (1)$$

where $\dot{\rho}_{0,\mathrm{BNS}}$ is the local BNS event rate density, $f(z)$ is the dimensionless redshift distribution factor, and z_max is the maximum redshift for BNS mergers. The comoving volume element $dV(z)/dz$ in Equation (1) is

$$\frac{dV}{dz} = \frac{c}{H_0} \frac{4\pi D_\mathrm{L}^2}{(1+z)^2 \sqrt{\Omega_\Lambda + \Omega_\mathrm{m}(1+z)^3}}, \quad (2)$$

[12] http://www.mephisto.ynu.edu.cn/site/

where c is the speed of light and $D_{\rm L}$ is the luminosity distance, which is expressed as

$$D_{\rm L} = (1+z)\frac{c}{H_0}\int_0^z \frac{dz}{\sqrt{\Omega_\Lambda + \Omega_{\rm m}(1+z)^3}}. \quad (3)$$

Recently, Abbott et al. (2021b) estimated the local BNS event rate density as $\dot{\rho}_{0,\rm BNS} = 320^{+490}_{-240}\ {\rm Gpc^{-3}\ yr^{-1}}$ based on the GW observations during the first half of the third observing (O3) run (see Mandel & Broekgaarden 2022, for a review of $\dot{\rho}_{0,\rm BNS}$). Hereafter, if not otherwise specified, $\dot{\rho}_{0,\rm BNS}$ used in our calculations is simply set as the median value of the GW constraint by the LIGO/Virgo Collaboration (LVC), i.e., $\dot{\rho}_{0,\rm BNS} \simeq 320\ {\rm Gpc^{-3}\ yr^{-1}}$.

BNS mergers can be thought as occurring with a delay timescale with respect to the star formation history. The Gaussian delay model (Virgili et al. 2011), log-normal delay model (Nakar et al. 2006; Wanderman & Piran 2015), and power-law delay model (Virgili et al. 2011; Hao & Yuan 2013; D'Avanzo et al. 2014) are the main types of delay time distributions. Sun et al. (2015) suggested that the power-law delay model leads to a wider redshift distribution of BNS mergers than the other two models, while recent observations of sGRBs by Zevin et al. (2022), Fong et al. (2022), O'Connor et al. (2022), and Nugent et al. (2022) supported the power-law delay. Although much debate remains, for simplicity, we only adopt the log-normal delay model as our merger delay model, and the analytical fitting expression of $f(z)$ is presented as Equation (A8) in Zhu et al. (2021d). With a known redshift distribution $f(z)$, we randomly simulate a group of $n_{\rm sim} = 5\times10^6$ BNS events in the universe based on Equation (1). For each BNS event, we then generate the EM emission. We briefly assume that all BNS events in the universe would only power three main types of EM signals, i.e., the jet afterglow, the kilonova, and the sGRB. We assume that cosmological kilonovae are AT2017gfo-like with the consideration of the viewing-angle effect, while the properties of afterglows are consistent with those of cosmological sGRB afterglows. The modeling details of the redshift distribution, jet afterglow, and kilonova emission of BNS mergers have been presented in Paper I. Our viewing-angle-dependent semi-analytical model of sGRB emission follows Song et al. (2019) and Yu et al. (2021). The signature of sGRBs depends on the on-axis equivalent isotropic energy E_0, the core half-opening angle $\theta_{\rm c}$, and the latitudinal viewing angle $\theta_{\rm view}$, while the afterglow emission has a dependence on four additional parameters, i.e., the number density of interstellar medium n, the power-law index of the electron distribution p, and the fractions of shock energy distributed in electrons, ε_e, and in magnetic fields, ε_B. Furthermore, the kilonova emission is only determined by $\theta_{\rm view}$. According to the distributions of the above parameters, as described in Paper I in detail, one can randomly generate the EM emission components for each simulated BNS event.

2.2. Classification of Detectable EM Counterparts

We divide the detectable events into two main groups based on the relative brightness of the detected kilonova and afterglow. If the peak kilonova flux is larger than 5 times the afterglow flux, i.e., $F_{\nu,\rm KN}(t_{\rm KN,p}) > 5F_{\nu,\rm AG}(t_{\rm KN,p})$, where $t_{\rm KN,p}$ is the peak time of the kilonova, we classify these events into the "kilonova-dominated sample." For such events, kilonova emission at the peak time would be at least 2 magnitudes brighter than that of the associated afterglow emission, so that this requirement can guarantee a clear kilonova signal for observers. For on-axis or near-on-axis afterglows, some bright kilonovae can appear detectable as an excess flux compared to the afterglow power-law decay, which are also defined as kilonova-dominated events. Other events are classified in the "afterglow-dominated sample," as the observed kilonova signals of these events may be ambiguous. In Paper I, we have shown that ∼50% on-axis and nearly on-axis afterglows are brighter than the associated kilonovae at the peak time. Thus, most of them would be afterglow dominated. Only at large viewing angles with $\sin\theta_{\rm v} \gtrsim 0.20$, would the EM signals of most BNS mergers be kilonova dominated, and some off-axis afterglows may emerge ∼5–10 days after the mergers.

Table 1
Sample for EM Counterparts of BNS Mergers

Sample	sGRB	Kilonova-dominated	Afterglow-dominated
Kilonova w/ sGRB	✓	✓	×
Kilonova w/o sGRB	×	✓	×
Afterglow w/ sGRB	✓	×	✓
Afterglow w/o sGRB	×	×	✓
sGRB only	✓	×	×

Some optically discovered EM counterparts of BNS mergers could be associated with sGRB observations. For the GW-triggered ToO searches, the observations of sGRBs can cooperate on the constraint on the sky location for BNS GW alerts, which would help us find the EM counterparts. On the basis of whether or not an sGRB is detected, we can further divide each sample into two subsamples, i.e., (1) kilonova-dominated sample: kilonova with (w/) an sGRB and kilonova without (w/o) an sGRB; (2) afterglow-dominated sample: afterglow w/ an sGRB and afterglow w/o an sGRB. Furthermore, a fraction of the BNS mergers may only be detected in the γ-ray band without any detection of an associated optical afterglow or kilonova. Thus, we totally define five subsamples for the EM counterparts of BNS mergers (see Table 1).

SGRBs are believed to be triggered if $F_\gamma > F_{\gamma,\rm limit}$, where F_γ is the γ-band flux for each BNS GW event (see Song et al. 2019; Yu et al. 2021, for details on the sGRB model) and $F_{\gamma,\rm limit}$ is the effective sensitivity limit for various γ-ray detectors. Many GRB detectors with quick response and wide FoVs, e.g., Swift (Gehrels et al. 2004), AstroSAT (Singh et al. 2014), Fermi (Meegan et al. 2009), and the Gravitational wave high-energy Electromagnetic Counterpart All-sky Monitor (GECAM; Zhang et al. 2019; Song et al. 2019), will work during O4. In our calculations, we simply set $F_{\gamma,\rm limit} \sim 2\times10^{-7}\ {\rm erg\ s^{-1}}$ in 50–300 keV, which is the effective sensitivity limit of the Fermi Gamma-ray Burst Monitor (GBM; Meegan et al. 2009) and GECAM (Zhang et al. 2019; Song et al. 2019), in view of the fact that Fermi-GBM and GECAM can nearly achieve an all-sky coverage to detect GRB events.[13]

[13] Compared with Fermi-GBM and GECAM, Swift-BAT (Gehrels et al. 2004; Lien et al. 2014) has a much lower sensitivity of $F_{\gamma,\rm limit} \sim 1\times10^{-8}\ {\rm erg\ s^{-1}}$ in 15–150 keV. However, unlike Fermi-GBM and GECAM that can nearly achieve an all-sky coverage, Swift-BAT's FoV is ∼1.4 sr. It is expected that the number of events with γ-ray triggers by Swift/BAT could be even lower than those by Fermi-GMB and GECAM due to its limited FoV (e.g., Song et al. 2019).

3. Detectability for Serendipitous Searches

In this section, we will introduce the method for the calculations of the EM detection rate by serendipitous observations, investigate the optimal search strategy, and show our simulated optically discovered detection rates of the kilonova-dominated and afterglow-dominated events for some specific survey projects. By considering the observations of sGRBs, the population properties for detectable EM events by serendipitous searches are detailedly discussed in what follows.

3.1. Method

Following Zhu et al. (2021d), we adopt a method of probabilistic statistical analysis to estimate the EM detection rate for BNS mergers. The probability that a single simulated event can be detected could be considered as the ratio of the survey area within the time duration (Δt) that the brightness of the associated EM signal is above the limiting magnitude ($m_{\rm limit}$) to the area of the celestial sphere ($\Omega_{\rm sph} = 41252.96\,{\rm deg}^2$). The maximum probability for a source to be detected is $\Omega_{\rm FoV}\dot{t}_{\rm ope}\Delta t/\Omega_{\rm sph}(n_{\rm exp}t_{\rm exp} + t_{\rm oth})$, where $\Omega_{\rm FoV}$ is the field of view (FoV) for the specific survey project, $\dot{t}_{\rm ope}$ is the average operation time per day, $n_{\rm exp}$ is defined as the exposure number for each visit, $t_{\rm exp}$ is the exposure time, and $t_{\rm other}$ is the rest of the time spent for each visit. However, high-cadence observations would restrict the survey area, which means that the probability of a source being detected by the high-cadence search would be a constant, i.e., $\Omega_{\rm FoV}\dot{t}_{\rm ope}t_{\rm cad}/\Omega_{\rm sph}(n_{\rm exp}t_{\rm exp} + t_{\rm oth})$, where the cadence time $t_{\rm cad}$ is defined as the interval between consecutive observations of the same sky area by a telescope. Furthermore, the event should appear in the sky coverage of the survey telescope so one can have a chance to discover it. Thus, we simply set an upper limit on the probability of a source to be detected, which is expressed as $\Omega_{\rm cov}/\Omega_{\rm sph}$, with $\Omega_{\rm cov}$ being the detectable sky coverage for a specific survey project. By counting the detection probabilities of all simulated events, one can write the EM detection rate for serendipitous observations as

$$\dot{N}_{\rm EM} \approx \frac{\dot{N}_{\rm BNS}}{n_{\rm sim}}\sum_{i=1}^{n_{\rm sim}}\min\left[\frac{\Omega_{\rm cov}}{\Omega_{\rm sph}}, \frac{\Omega_{\rm FoV}\dot{t}_{\rm ope}\min(t_{\rm cad}, \Delta t_i)}{\Omega_{\rm sph}(n_{\rm exp}t_{\rm exp} + t_{\rm oth})}\right]. \quad (4)$$

We roughly assume that the average operation time per day is $\dot{t}_{\rm ope} \approx 6\ {\rm hr\ day}^{-1}$ for all survey projects except for SiTian. The time spent for each visit $t_{\rm oth}$ is dependent on the technical performance of the specific survey project and the different search strategy. Because $t_{\rm oth}$ is uncertain, we set it as a constant for each survey project, i.e., $t_{\rm oth} = 15$ s.

In order to reject the supernova background and other rapid-evolving transients, in Paper I, we showed that one can use the unique color evolution of kilonovae and afterglows to identify them among the observed transients. We require that the judgment condition for the detection of the kilonova and/or afterglow by a serendipitous search is that "two different exposure filters have at least two detection epochs." It would be $n_{\rm exp} = 1$ for Mephisto and SiTian as these two survey projects can achieve simultaneous imaging in three bands,[14] while $n_{\rm exp} = 2$ for ZTF, WFST, and LSST.

[14] The optical system of Mephisto consists of a modified Ritchey–Chrétien design with three refractive correctors and three cubes for beam splitting so it is capable of simultaneously imaging the same patch of sky in three bands (X.-Z. Er et al. 2023, in preparation). SiTian is composed of a number of "units", namely, three 1 m class Schmidt telescopes (see Section 3.4 for more details). Both of them can achieve simultaneous imaging in three bands.

The values of some technical parameters, including the expected limiting magnitude (which is a logarithmic function of the exposure time in each band), the FoV, and the detectable sky coverage, for the survey telescopes we considered are presented in Table 2. As examples, we also list the g-band limiting magnitudes $m_{g,\rm limit}$ for different exposure times of $t_{\rm exp} = 30, 180, 300$ s for the survey telescopes in Table 2. Thus, survey telescopes with apertures smaller than those of ZTF and SiTian can have a limiting magnitude of $m_{\rm limit} \lesssim 20$ mag. The detection depths of ZTF and SiTian lie in the range $20\ {\rm mag} \lesssim m_{\rm limit} \lesssim 22$ mag. A range of $22\ {\rm mag} \lesssim m_{\rm limit} \lesssim 24$ mag applies to Mephisto and WFST, and $24 \lesssim m_{\rm limit} \lesssim 26$ mag can be only achieved by LSST.

3.2. Δt_{EM} and Cadence Time Selection

As listed in Table 3, we show the 90% credible regions of two timescales, i.e., $\Delta t_{\rm KN}$ and $\Delta t_{\rm AG}$, with different filters and different limiting magnitudes. These two parameters are, respectively, defined as the timescales during which the brightness of the associated kilonova and afterglow is above the limiting magnitude in different bands. Because the *gri* bands are the common filters used by various survey projects, we only show the probability density functions of $\Delta t_{\rm KN}$ and $\Delta t_{\rm AG}$ with different searching magnitudes in these three bands in Figure 1.

As shown in Table 3, for a limiting magnitude of $m_{\rm limit} \leqslant 19$ mag, the values of $\Delta t_{\rm KN}$ may be imprecise, due to the limited amount of available data. For $m_{\rm limit} \geqslant 20$ mag, one can see that the median value of $\Delta t_{\rm KN}$ is ∼0.6–1.4 days in the optical and ∼1.4–2.1 days in the infrared, which may be uncorrelated with the limiting magnitude $m_{\rm limit}$. If the observer wants to achieve at least two detection epochs for at least 50% of the observable kilonova signals, the cadence time $t_{\rm cad}$ should be less than half of the median value of $\Delta t_{\rm KN}$. This means $t_{\rm cad}$ should be $t_{\rm cad} \lesssim 0.3$–0.7 days if one uses the optical band to search for kilonovae and $t_{\rm cad} \lesssim 0.7$–1.0 days in an infrared-band search for all survey projects.

Unlike $\Delta t_{\rm KN}$, there exists a positive correlation between $\Delta t_{\rm AG}$ and $m_{\rm limit}$, as shown in Table 3. The median value of $\Delta t_{\rm KN}$ would always be larger than $\Delta t_{\rm AG}$ if $m_{\rm limit} \lesssim 24$ mag. Thus, LSST, which has a limiting magnitude of $m_{\rm limit} \gtrsim 24$ mag, can find ≳50% detectable afterglows brighter than the searching limiting magnitude by adopting a cadence to search for kilonovae. As shown in Figure 1, the probability density function of $\Delta t_{\rm AG}$ is significantly higher than that of $\Delta t_{\rm KN}$, especially for searching with a relatively shallow limiting magnitude in a bluer filter band. Thus, it may be easier to discover optical afterglows by adopting the cadence of searching for kilonovae.

3.3. Optimal Search Strategy

We show the detection rates of the kilonova-dominated and afterglow-dominated samples for ZTF, Mephisto, WFST, and LSST in Figures 2 and 3, by considering exposure times from 30 to 300 s and five different cadence timescales, $t_{\rm cad} = 0.5$ hr, 1 hr, 3 hr, 1 day, and 2 days. The results shown in Figures 2 and 3 are obtained considering only the *gri* bands as these three bands are commonly used for these survey telescopes. Because SiTian is an integrated network of dozens of survey and follow-up telescopes, its survey strategy should largely differ from those of other survey projects. We give a separate calculation of the EM detection rates for SiTian in Section 3.4.

Table 2
Summary Technical Information for Each Survey

Telescope	$m_{\rm limit} = a \times t_{\rm exp}^{b}$						$t_{\rm exp}$/s	$m_{g,\rm limit}$/mag	FoV/deg^2	Sky Coverage/deg^2	References
ZTF	g		r		i		30	20.3	47.7	30,000	(1)
	18.62		18.37		17.91		180	21.3			
	0.026		0.026		0.027		300	21.6			
Mephisto	u	v	g	r	i	z	30	22.4	3.14	26,000	(2)
	18.45	18.54	19.91	19.91	19.68	18.71	180	23.8			
	0.043	0.042	0.034	0.032	0.030	0.033	300	24.2			
WFST	u	g	r	i	z	w	30	23.0	6.55	20,000	(3)
	20.70	21.33	21.13	20.46	19.41	21.33	180	23.9			
	0.022	0.022	0.022	0.023	0.024	0.022	300	24.2			
LSST	u	g	r	i	z	y	30	25.1	9.6	20,000	(4)
	22.03	23.60	22.54	21.73	21.83	21.68	180	25.9			
	0.025	0.018	0.023	0.030	0.031	0.032	300	26.2			
SiTian[a]	g		r		i		30	20.3	600	30,000	(5)
	18.62		18.37		17.91		180	21.3			
	0.026		0.026		0.027		300	21.6			

Notes. The columns are: [1] the survey project; [2] the search limiting magnitude $m_{\rm limit}$ as a logarithmic function of the exposure time $t_{\rm exp}$ in different bands for specific survey projects (parameters a and b are, respectively, the values at the second and third subrows of each row); [3] the exposure time $t_{\rm exp}$; [4] the g-band limiting magnitude $m_{g,\rm limit}$ corresponding to different exposure times; [5] the FoV $\Omega_{\rm FoV}$; [6] the detectable sky coverage $\Omega_{\rm cov}$; [7] References: (1) Bellm et al. (2019), Masci et al. (2019), (2) X.-Z. Er et al. (2023, in preparation), Lei et al. (2021), (3) X. Kong et al. (2023, in preparation), Shi et al. (2018), (4) LSST Science Collaboration et al. (2009), (5) Liu et al. (2021).

[a] The technical specification of the limiting magnitude in the g-band stacked images for SiTian is similar to that for ZTF (Liu et al. 2021). SiTian would simultaneously observe the same visit in three different filters (u, g, i). Due to the lack of the technical information in u and i band of SiTian, we simply use the technical information of ZTF in the gri bands to calculate the EM detection rates by SiTian.

Table 3
Time During which the Brightness of the EM Counterpart is above the Limiting Magnitude

Filter	Parameter	$m_{\rm limit} = 18$ mag	19 mag	20 mag	21 mag	22 mag	23 mag	24 mag	25 mag	26 mag
u	$\Delta t_{\rm KN}$	...	$0.67^{+0}_{-0.67}$	$0.65^{+0.77}_{-0.65}$	$0.82^{+0.63}_{-0.72}$	$0.8^{+1.1}_{-0.6}$	$0.7^{+1.4}_{-0.6}$	$0.7^{+1.3}_{-0.5}$	$0.7^{+1.2}_{-0.6}$	$0.8^{+1.2}_{-0.6}$
	$\Delta t_{\rm AG}$	$0.12^{+0.55}_{-0.11}$	$0.14^{+0.68}_{-0.12}$	$0.18^{+0.91}_{-0.16}$	$0.2^{+1.3}_{-0.2}$	$0.3^{+1.9}_{-0.3}$	$0.4^{+3.0}_{-0.4}$	$0.6^{+4.7}_{-0.5}$	$0.9^{+7.5}_{-0.8}$	2^{+12}_{-1}
g	$\Delta t_{\rm KN}$	$0.83^{+0}_{-0.83}$	$0.7^{+1.1}_{-0.7}$	$1.3^{+0.8}_{-1.2}$	$1.2^{+1.4}_{-1.0}$	$1.2^{+1.9}_{-0.9}$	$1.1^{+1.7}_{-0.8}$	$1.0^{+1.7}_{-0.7}$	$0.9^{+1.8}_{-0.7}$	$0.9^{+1.9}_{-0.7}$
	$\Delta t_{\rm AG}$	$0.12^{+0.58}_{-0.11}$	$0.15^{+0.73}_{-0.13}$	$0.19^{+0.97}_{-0.17}$	$0.2^{+1.4}_{-0.2}$	$0.3^{+2.1}_{-0.3}$	$0.4^{+3.3}_{-0.4}$	$0.6^{+5.2}_{-0.5}$	$1.0^{+8.1}_{-0.9}$	2^{+13}_{-2}
v	$\Delta t_{\rm KN}$	$1.4^{+0}_{-1.4}$	$0.7^{+1.1}_{-0.6}$	$1.1^{+1.5}_{-0.8}$	$1.0^{+2.4}_{-0.8}$	$1.1^{+2.3}_{-0.7}$	$1.0^{+2.0}_{-0.8}$	$1.1^{+1.9}_{-0.8}$	$1.2^{+2.0}_{-0.9}$	$1.3^{+1.9}_{-0.7}$
	$\Delta t_{\rm AG}$	$0.13^{+0.60}_{-0.12}$	$0.15^{+0.77}_{-0.13}$	$0.2^{+1.0}_{-0.2}$	$0.2^{+1.5}_{-0.2}$	$0.3^{+2.2}_{-0.3}$	$0.4^{+3.4}_{-0.4}$	$0.6^{+5.4}_{-0.6}$	$1.0^{+8.6}_{-1.0}$	2^{+13}_{-2}
w	$\Delta t_{\rm KN}$	$0.5^{+1.1}_{-0.5}$	$0.89^{+0.88}_{-0.60}$	$1.2^{+1.6}_{-0.9}$	$1.2^{+2.3}_{-0.8}$	$1.2^{+2.3}_{-0.8}$	$1.1^{+2.3}_{-0.8}$	$1.1^{+2.2}_{-0.8}$	$1.2^{+2.1}_{-0.8}$	$1.3^{+2.0}_{-1.0}$
	$\Delta t_{\rm AG}$	$0.13^{+0.61}_{-0.12}$	$0.15^{+0.78}_{-0.13}$	$0.2^{+1.0}_{-0.2}$	$0.2^{+1.5}_{-0.2}$	$0.3^{+2.2}_{-0.3}$	$0.4^{+3.5}_{-0.4}$	$0.6^{+5.5}_{-0.6}$	$1.1^{+8.7}_{-1.0}$	2^{+14}_{-2}
r	$\Delta t_{\rm KN}$	$0.7^{+1.0}_{-0.7}$	$1.07^{+0.88}_{-0.69}$	$1.3^{+1.7}_{-1.0}$	$1.2^{+2.5}_{-0.8}$	$1.1^{+2.4}_{-0.8}$	$1.3^{+2.1}_{-0.9}$	$1.3^{+2.2}_{-0.9}$	$1.2^{+2.4}_{-0.9}$	$1.3^{+2.4}_{-0.9}$
	$\Delta t_{\rm AG}$	$0.13^{+0.63}_{-0.12}$	$0.15^{+0.79}_{-0.13}$	$0.2^{+1.1}_{-0.2}$	$0.3^{+1.5}_{-0.2}$	$0.3^{+2.3}_{-0.3}$	$0.4^{+3.6}_{-0.4}$	$0.7^{+5.6}_{-0.6}$	$1.1^{+8.9}_{-1.0}$	2^{+14}_{-2}
i	$\Delta t_{\rm KN}$	$0.7^{+1.9}_{-0.7}$	$1.3^{+1.3}_{-0.7}$	$1.5^{+2.2}_{-1.3}$	$1.4^{+3.1}_{-0.9}$	$1.3^{+2.6}_{-1.0}$	$1.3^{+2.4}_{-1.0}$	$1.4^{+2.4}_{-0.9}$	$1.4^{+2.5}_{-1.0}$	$1.7^{+2.6}_{-1.2}$
	$\Delta t_{\rm AG}$	$0.13^{+0.67}_{-0.12}$	$0.16^{+0.84}_{-0.14}$	$0.2^{+1.1}_{-0.2}$	$0.3^{+1.6}_{-0.2}$	$0.3^{+2.4}_{-0.3}$	$0.5^{+3.8}_{-0.4}$	$0.7^{+6.0}_{-0.6}$	$1.1^{+9.4}_{-1.1}$	2^{+15}_{-2}
z	$\Delta t_{\rm KN}$	$0.8^{+2.3}_{-0.8}$	$1.6^{+1.6}_{-1.1}$	$2.0^{+2.3}_{-1.4}$	$1.8^{+3.0}_{-1.3}$	$1.8^{+2.7}_{-1.3}$	$1.8^{+2.6}_{-1.3}$	$1.6^{+2.9}_{-1.1}$	$1.6^{+3.1}_{-1.2}$	$1.7^{+2.8}_{-1.3}$
	$\Delta t_{\rm AG}$	$0.14^{+0.69}_{-0.13}$	$0.16^{+0.89}_{-0.14}$	$0.2^{+1.2}_{-0.2}$	$0.3^{+1.7}_{-0.2}$	$0.4^{+2.6}_{-0.3}$	$0.5^{+4.0}_{-0.4}$	$0.7^{+6.3}_{-0.7}$	1^{+10}_{-1}	2^{+15}_{-2}
y	$\Delta t_{\rm KN}$	$1.0^{+2.2}_{-1.0}$	$1.8^{+1.5}_{-1.7}$	$2.1^{+2.2}_{-1.7}$	$1.8^{+3.6}_{-1.4}$	$1.9^{+2.9}_{-1.4}$	$1.9^{+2.7}_{-1.4}$	$1.9^{+2.9}_{-1.4}$	$1.9^{+2.8}_{-1.5}$	$1.7^{+3.2}_{-1.4}$
	$\Delta t_{\rm AG}$	$0.14^{+0.71}_{-0.12}$	$0.17^{+0.90}_{-0.15}$	$0.2^{+1.2}_{-0.2}$	$0.3^{+1.8}_{-0.2}$	$0.4^{+2.6}_{-0.3}$	$0.5^{+4.1}_{-0.5}$	$0.8^{+6.5}_{-0.7}$	1^{+10}_{-1}	2^{+16}_{-2}

Note. The values are the timescales during which the brightness of the associated kilonova ($\Delta t_{\rm KN}$) and afterglow ($\Delta t_{\rm AG}$) is above the 5σ limiting magnitude in different bands with a 90% interval.

As shown in Figure 2, for each survey project, the difference in the detection rates of the kilonova-dominated events between different bands seems very small, of the order of unity. For the cadence choice, we find that a one-day cadence strategy can always discover the highest number of kilonovae. Regarding the choice of the exposure time, the kilonova detection rates by ZTF, WFST, and LSST would decline as the exposure time increases. On the contrary, a longer exposure time can lead to the discovery of more kilonova events for Mephisto, although the increase in the amount of discovered kilonovae for longer

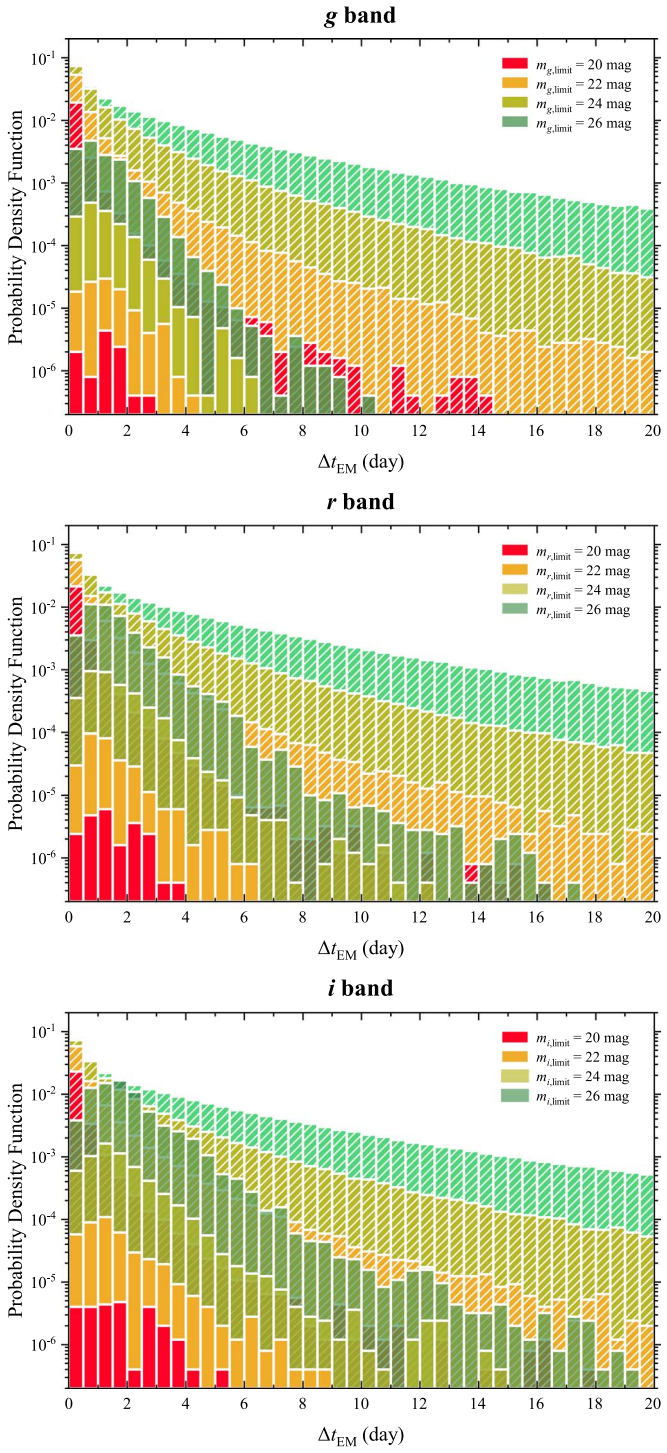

Figure 1. The crimson, orange, yellow green, and green histograms are the probability density functions of $\Delta t_{\rm KN}$ (solid histograms) and $\Delta t_{\rm AG}$ (striped histograms) for limiting magnitudes of $m_{\rm limit} = 20$, 22, 24, and 26 mag, in the g band (top panel), r band (medium panel), and i band (bottom panel). The bin width of the histograms is set to $\Delta = 0.5$ day.

exposure times is not significant. The simultaneous imaging in three bands by Mephisto is the reason for the difference in the detection rates between Mephisto and other survey projects. To sum up, a one-day cadence strategy with a ∼30 s exposure time is recommended to achieve optimal search for kilonovae. Based on Figure 2, the maximum kilonova detection rates for ZTF, Mephisto, WFST, and LSST are $\sim 0.3\,{\rm yr}^{-1}$, $\sim 0.6\,{\rm yr}^{-1}$, $\sim 1\,{\rm yr}^{-1}$, and $20\,{\rm yr}^{-1}$, respectively.

For afterglow-dominated events, there is no significant difference between searching in the optical and in the infrared bands for each survey project. The detection rates would drop with the increase in the exposure time. By adopting the optimal search strategy for kilonovae, one can also discover many afterglows from BNS mergers whose detection rate is much higher than that of kilonovae. For this case, the afterglow detection rates for ZTF, Mephisto, WFST, and LSST are $\sim 50\,{\rm yr}^{-1}$, $\sim 60\,{\rm yr}^{-1}$, $\sim 100\,{\rm yr}^{-1}$, and $\sim 800\,{\rm yr}^{-1}$, respectively.

3.4. Optimal Search Strategy for SiTian

SiTian (Liu et al. 2021; Yang et al. 2022a) is composed of a number of "units" deployed partly in China and partly at various sites around the world. Each unit includes three 1 m class Schmidt telescopes with a FoV of $\Omega_{\rm FoV} = 25\,{\rm deg}^2$, which will simultaneously observe the same visit in three different optical filters. There will be also three or four 4 m class telescopes for spectral identification and follow-up studies within the project.

SiTian at full design will scan at least 10,000 $\deg^2$ of sky every 30 minutes, down to a detection limit of $g \approx 21$ mag with an exposure time of ∼1 minute using at least 14 units in China. Furthermore, at least 10 units outside China can survey an additional $\sim 20{,}000\,{\rm deg}^2$ with a slightly lower cadence (a few hours). Based on this fiducial search plan of SiTian, we change the cadence time and exposure time for all of units to explore the optical search strategy of SiTian, while preserving the same sky coverage.

The results of the EM detection rates for SiTian are shown in Table 4. We show that SiTian can detect $\sim 2 \times 10^3\,{\rm yr}^{-1}$ afterglow-dominated events. The detection rate of kilonova-dominated events is $\sim$(2–4) $\rm yr^{-1}$ by adopting the fiducial search plan of SiTian. As kilonovae are very faint, a better search strategy would be to increase the exposure time of the telescopes with the expense of losing the cadence. The detection rate of kilonova-dominated events would slightly rise to $\sim$(3–7) $\rm yr^{-1}$ if an exposure time of 165 s is used.

3.5. Population Properties of Detectable EM Events by Serendipitous Observations

By adopting an optimal serendipitous search strategy, i.e., a one-day cadence strategy, we show the redshift distributions of the detectable EM signals for a g-band limiting magnitude of $m_{g,\rm limit} = 20$, 22, 24, and 26 mag in Figure 4. As for each detectable EM signal, we randomly simulate the detection epochs 1000 times and calculate the median difference value between these detection epochs as the fading rate. Figure 5 shows the distributions of the fading rate for detectable EM signals. For the same search depth of each filter, there is no significant difference between searching in different bands. It is important to note that we collect all EM events with $t_{\rm cad} \geqslant 1$ day when we calculate the redshift distributions of the detectable EM signals; so the distributions shown in Figure 4 do not consider their detection probabilities.

For a limiting magnitude of $m_{\rm limit} = 20$ mag, the most likely EM counterpart of BNS mergers to be detected is individual sGRB emission. Due to this relatively shallow search depth, afterglow emissions associated with these individual sGRBs could have at most one recorded epoch. In this case, it may be hard to establish the link between the sGRBs and the associated afterglows by optically

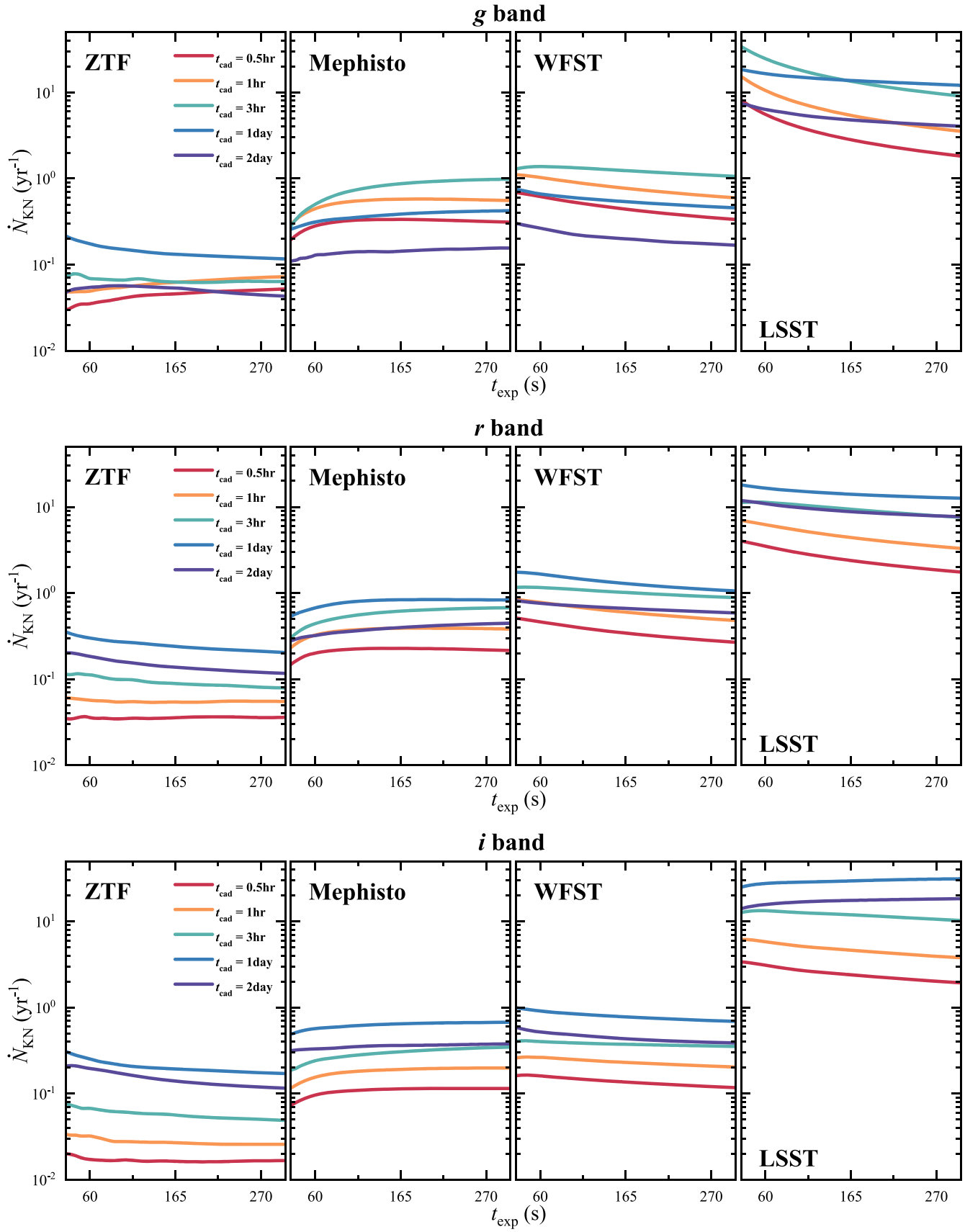

Figure 2. Detection rates of the kilonova-dominated sample as functions of the exposure time t_{exp} and cadence time t_{cad} for serendipitous observations. Four survey projects, including ZTF, Mephisto, WFST, and LSST (panels from left to right), are considered. The panels from top to bottom represent events of the kilonova-dominated sample to be detected in the *g*, *r*, and *i* bands, respectively. The red, orange, green, blue, and violet lines are the detection rates adopting cadence searching strategies of $t_{cad} = 0.5$ hr, 1 hr, 3 hr, 1 day, and 2 days, respectively.

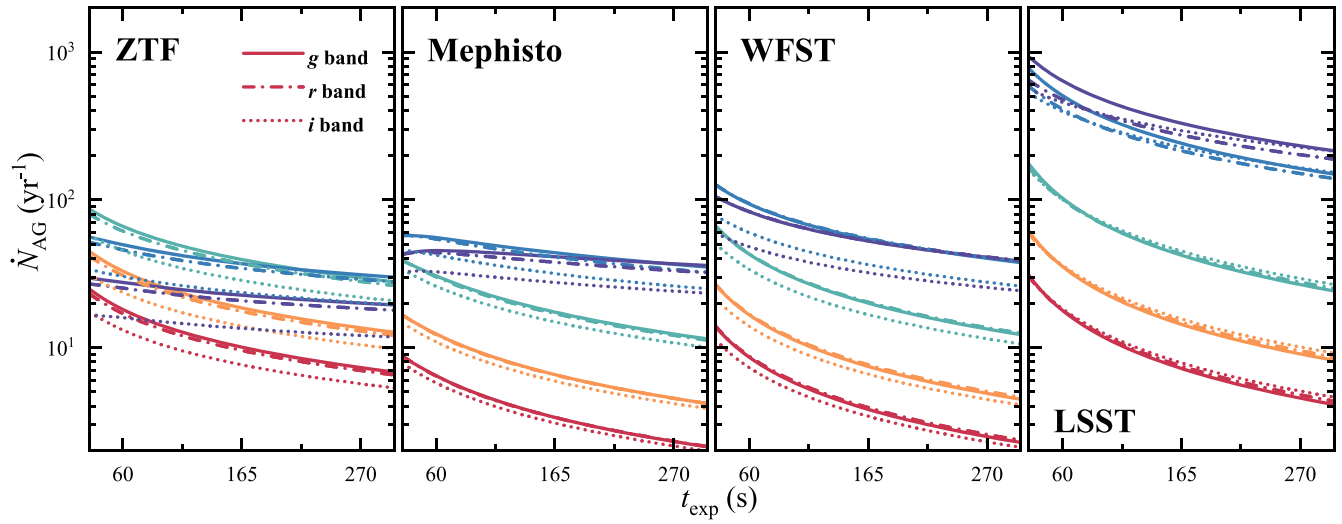

Figure 3. Similar to Figure 2, but for the detection rates of the afterglow-dominated sample. The solid, dashed–dotted, and dotted lines represent the detection rates in the g, r, and i bands, respectively.

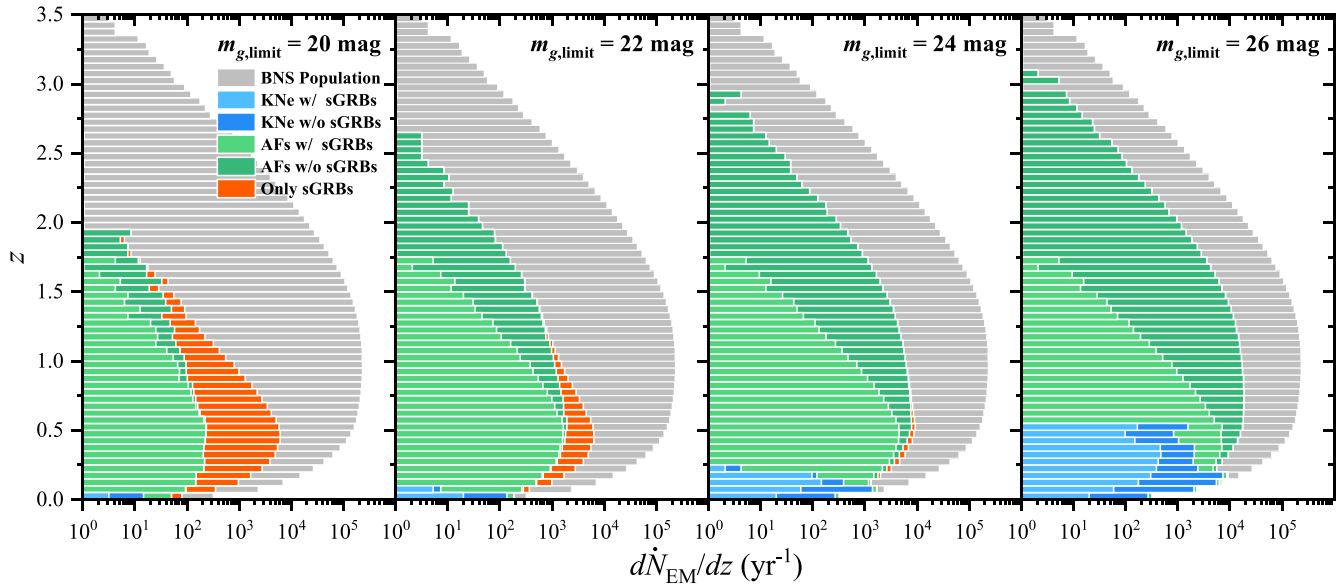

Figure 4. Redshift distributions of the detectable EM signals by serendipitous searches for a g-band limiting magnitude of $m_{g,\rm limit} = 20$, 22, 24, and 26 mag (panels from left to right). The gray histograms are the redshift distributions of the simulated cosmological BNS population. The light blue, dark blue, light green, dark green, and orange histograms represent the redshift distributions for the delectable samples of kilonovae w/sGRBs, kilonovae w/o sGRBs, afterglows w/sGRBs, afterglows w/o sGRBs, and sGRBs only, respectively. The bin width of the histograms is set to $\Delta = 0.05$.

Table 4
EM Detection Rates for SiTian

$t_{\rm exp}$/s	$\Omega_{\rm FoV,1}$/deg^2	$t_{\rm cad,1}$/minutes	$\Omega_{\rm FoV,2}$/deg^2	$t_{\rm cad,2}$/minutes	$\dot{N}_{\rm KN}$/yr^{-1}			$\dot{N}_{\rm AG} \times 10^3$/yr^{-1}		
					g	r	i	g	r	i
45 (fiducial)	350	30	250	80	2.0	3.4	3.6	1.5	1.7	1.9
75		45		120	2.4	4.3	4.7	1.7	1.9	2.0
105		60		160	2.7	5.0	5.6	1.7	1.9	2.1
165		90		240	3.0	5.8	7.1	1.7	1.9	2.0

Note. We assume that the time between two visits is $t_{\rm oth} = 15$ s. The operation times for units in China and outside China are assumed to be $t_{\rm ope} = 8$ hr day^{-1} and 16 hr day^{-1}, respectively. The columns are: [1] the exposure time; [2] the total FoV of SiTian units in China; [3] the corresponding cadence time for SiTian units in China; [4] the total FoV of SiTian units outside China; [5] the corresponding cadence time for SiTian units outside China; [6]–[8] the detection rates of kilonova-dominated events in the *gri* bands; [9]–[11] the detection rates of afterglow-dominated events in the *gri* bands.

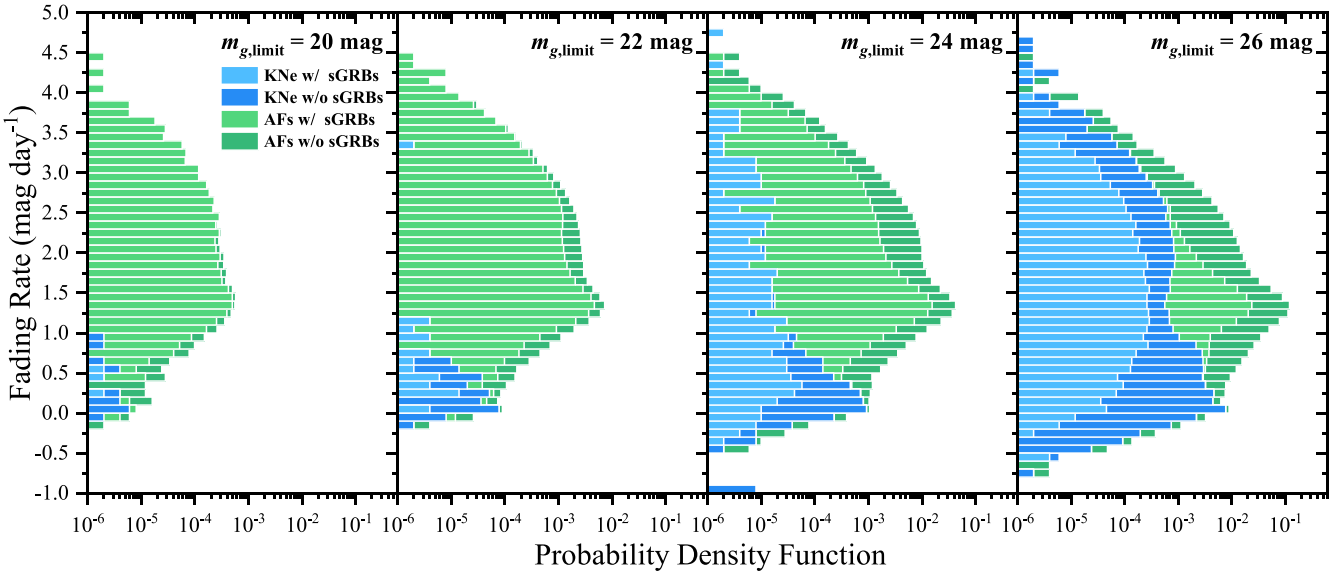

Figure 5. Similar to Figure 4, but for the g-band fading rates of the detectable EM signals. The bin width of the histograms is set to $\Delta = 0.1$ mag day^{-1}.

serendipitous searches. Detectable afterglow emissions should be much easier to be discovered than kilonova emissions. However, these optical afterglows should always be associated with sGRB emissions. The most probable detectable redshift for these individual sGRBs and GRB-associated afterglows is $z \sim 0.5$, which is consistent with the observations (e.g., Fong et al. 2015). Some detectable orphan afterglows with much lower detection rates could take place at a range of $z \gtrsim 0.75$. In our simulations, the largest distance of detectable kilonovae is $z_{\rm max} \sim 0.02$ ($D_{\rm L,max} \sim 80$ Mpc). Most (∼80%–90%) of these detectable kilonovae are expected to be discovered individually without the detection of accompanied sGRB emissions.

The improvement in the search depth would lead to a proportionate decrease in the number of individual detectable sGRB events. If $m_{\rm limit} \gtrsim 22$ mag, more near-on-axis orphan afterglows and nearby off-axis orphan afterglows can be discovered, which would become the primary detectable EM counterparts of BNS mergers. For a limiting magnitude of $m_{\rm limit} \gtrsim 24$ mag, one can always find the associated afterglow and kilonova emissions after sGRB triggers by optically serendipitous searches. Due to the limited instrument sensitivity of γ-ray telescopes, the largest distance of sGRB-associated afterglows and kilonovae is $z_{\rm max} \sim 1.75$. We note that this simulated largest distance of sGRB triggers is obtained by adopting the effective sensitivity limit of Fermi-GBM and GECAM. A few Swift sGRBs were found to have photometric redshifts of $z \gtrsim 2$, as presented by Nugent et al. (2022), because the Swift Burst Alert Telescope (BAT) has a lower sensitivity compared with Fermi-GBM and GECAM, and hence a deeper detection depth. With the increase in the search depth, kilonovae would play a leading role in nearby detectable EM counterparts. For limiting magnitudes of $m_{g,\rm limit} = 22$, 24, and 26 mag, the median (largest) distances of these detectable kilonovae are $z = 0.04$, 0.1, and 0.25 ($z_{\rm max} = 0.06$, 0.21, and 0.55), respectively. The search depth has little effect on the ratio between detectable kilonovae w/sGRBs and kilonovae w/o sGRBs.

The fading rates of detectable afterglows always peak at ∼1.3 mag day^{-1} and have a wide distribution between ∼−0.5 mag day^{-1} and ∼4.5 mag day^{-1}. Comparing with afterglows, kilonova-dominated events have more slow-evolving light curves. Their fading rates peak at ∼0–0.1 mag day^{-1}. For a limiting magnitude of $m_{\rm limit} \lesssim 22$ mag, the fading rates of kilonovae are in the range from −0.25 day^{-1} to ∼1 mag day^{-1}. As shown in Figure 5, by adopting a limiting magnitude of $m_{\rm limit} \gtrsim 24$ mag ($m_{\rm limit} \gtrsim 26$ mag), some fast-evolving sGRB-associated kilonovae (kilonovae w/sGRBs and kilonovae w/o sGRBs) with a fading rate of $\gtrsim$1 mag day^{-1} can be discovered. For these fast-evolving kilonova events, their early-stage observations would be contributed by the associated afterglows while the kilonova emissions would lead to late-stage observations.

Table 5
O3 Duty Cycle

Online Detector	$P_{\rm duty}$
HLV	46.75%
HL	14.80%
HV	9.68%
LV	11.8%
H	3.06%
L	2.94%
V	7.59%
None	3.35%

4. Detectability for Target-of-opportunity Observations of GW Triggers

4.1. GW Detectability Method

It is expected that two Advanced LIGO detectors (H1 and L1) in the USA (Harry & LIGO Scientific Collaboration 2010; LIGO Scientific Collaboration et al. 2015), the Advanced Virgo detector (V1) in Europe (Acernese et al. 2015), and the KAGRA detector (K1) in Japan (Aso et al. 2013; Kagra Collaboration et al. 2019) will start the fourth observation run (O4) together in 2023. Hereafter, the network composed of these second-generation detectors is referred to as the "HLV era". Here, the sensitivities of H1, L1, and V1 in the HLV era are adopted as their respective

Table 6
GW Detection Results

Case	Era	$\dot{N}_{\rm GW}/{\rm yr}^{-1}$ ($\dot{N}_{\rm GW}/\dot{N}_{\rm BNS}$)	z ($D_{\rm L}$/100 Mpc)	$z_{\rm max}$ ($D_{\rm L,max}$/100 Mpc)	$\log_{10}(\Omega_{\rm GW}/{\rm deg}^2) = a \times \log_{10}(z) + b$	
					a	b
HLV (O3)	2nd	$2.4^{+3.6}_{-1.8}$ (0.001%)	$0.025^{+0.025}_{-0.013}$ ($1.1^{+1.2}_{-0.5}$)	0.062 (2.9)	⋯	⋯
HLV (O4)	2nd	11^{+17}_{-8} (0.004%)	$0.040^{+0.025}_{-0.025}$ ($1.8^{1.2}_{1.1}$)	0.084 (4.0)	1.93	$4.02^{+0.85}_{-0.42}$
PlusNetwork	2.5th	210^{+320}_{-160} (0.08%)	$0.099^{+0.050}_{-0.055}$ ($4.7^{+2.6}_{-2.7}$)	0.190 (9.5)	1.87	$2.85^{+0.45}_{-0.55}$
LIGO Voyager	3rd	$1.8^{+2.8}_{-1.4} \times 10^3$ (0.73%)	$0.22^{+0.12}_{-0.13}$ ($11.0^{+7.4}_{-6.7}$)	0.43 (24.3)	⋯	⋯
ET&CE	3rd	$2.4^{+3.6}_{-1.8} \times 10^5$ (90.7%)	$0.97^{+0.71}_{-0.57}$ (65^{+64}_{-43})	3.77 (343)	2.00	$0.85^{+0.69}_{-0.46}$

Note. The GW detection rates and luminosity distance distributions for detectable GWs in the second-generation era are simulated by adopting the exact duty cycle labeled in Table 5, while GW detection results in the 2.5th- and third-generation eras are obtained under ideal operation conditions. The columns are: [1] the case of different generation eras; [2] the generation of GW detectors; [3] the median GW detection rates adopting a 90% interval and a local event rate density of $\dot{\rho}_{0,\rm BNS} = 320^{+490}_{-240}\ {\rm Gpc}^{-3}\ {\rm yr}^{-1}$ (Abbott et al. 2021b), while the numbers in brackets are the corresponding detectable proportions of the number of BNS mergers per year in the universe ($\dot{N}_{\rm BNS}$); [4] the median detectable redshifts and detectable luminosity distances at 90% intervals; [5] the maximum detectable redshifts and detectable luminosity distances; [6] the GW sky localizations as function of z, where a and b are fitting parameters.

design sensitivities (Abbott et al.2020a) because their sensitivities are dynamic and change over time,[15] while K1 is ignored in our simulations as it will work toward improving most of time during O4.[16] The second-generation detectors would finish their upgrade to 2.5th-generation detectors in ∼2025. The subsequent upgrades of Advanced LIGO, Advanced Virgo, and KAGRA are called Advanced LIGO Plus (A+; Miller et al. 2015), Advanced Virgo Plus (AdV+; Abbott et al. 2020a), and KAGRA+ (Michimura et al. 2020). Hereafter, we refer to the era during which these four detectors will upgrade to 2.5th-generation detectors as the "PlusNetwork era." After ∼2030, the third-generation GW detectors are expected to start their observation. The currently proposed third-generation detector plans include LIGO Voyager (Adhikari et al. 2020) as a possible upgrade upon LIGO A+ (strictly speaking, it is more like quasi-third generation, but as its sensitivity is much higher than that of the 2.5th-generation detectors, we classify it as 3G for convenience), the Einstein Telescope (ET) in Europe (Punturo et al. 2010a, 2010b; Maggiore et al. 2020), and the Cosmic Explorer (CE) in the USA (Reitze et al. 2019). Due to the as-yet undetermined locations of ET and CE, we directly place ET at the current Virgo detector position and two CE detectors at the current H1 and L1 positions, according to convention (Vitale & Evans 2017; Vitale & Whittle 2018).

For each BNS system, we randomly simulate the masses of individual NSs based on the observationally derived mass distribution of Galactic BNS systems, i.e., a normal distribution $M_{\rm NS}/M_\odot \sim \mathcal{N}(1.32, 0.11^2)$ (Lattimer 2012; Kiziltan et al. 2013). The NS equation of state (EoS) DD2 (Typel et al. 2010), which is one of the stiffest EoS allowed by present constraints (e.g., Gao et al. 2016; Abbott et al. 2019), is adopted. With known $M_{\rm NS}$, z, and EoS, we use the `IMRPhenomPv2_NRTidalv2` (Dietrich et al. 2019) waveform model to simulate the GW waveform in the geocentric coordinate system, and then project it to different detectors to obtain the detector-frame strain signal. The optimal signal-to-noise ratio (S/N) can be obtained by

$$\rho^2_{\rm opt} = 4\int_{f_{\rm min}}^{f_{\rm max}} \frac{|\tilde{h}(f)|^2}{S_n(f)} df = \int_{f_{\rm min}}^{f_{\rm max}} \frac{(2|\tilde{h}(f)|\sqrt{f})^2}{S_n(f)} d\ \ln(f), \quad (5)$$

where f is the frequency, $\tilde{h}(f)$ is the strain signal in the frequency domain, and $S_n(f)$ is the one-sided power spectral density of the GW detector, which is the square of the amplitude spectral density (ASD). The ASD for each detector is shown in the Appendix. We set the maximum frequency $f_{\rm max}$ as 2048 Hz. The low-frequency cutoff $f_{\rm min}$ is set to 20 Hz for O3; 10 Hz for the second- and 2.5th-generation detectors (Miller et al. 2015), and LIGO Voyager (Adhikari et al. 2020); 5 Hz for CE (Reitze et al. 2019) and 1 Hz for ET (Punturo et al. 2010a). We use the optimal S/N to approximate the matched filtering S/N of the GW signal detected by each detector, and then calculate the network S/N of the entire detector network, i.e., the root sum squared of the S/N of all detectors. In each GW era, when the S/N for a single detector is greater than the threshold of 8 and the network S/N is greater than 12, we expect that the corresponding GW signal is detected.

We consider the exact duty cycle of O3 (see Table 5), calculated following the timeline released from LVC,[17] to simulate the GW observations of BNS mergers in O3 and O4. In view of the significant technology upgrades in GW detections and the fact that more detectors will join GW campaigns, the duty cycle in the 2.5th- and third-generation detector networks could be highly uncertain. Thus, we only calculate their best cases, i.e., "all detectors in the

[15] We show differences between the design sensitivity curves we use and the latest sensitivity curves released on 2022 April 6 in Figure 13 of the Appendix. Based on these latest sensitivity curves, our simulations of the GW detection rate in O4 might be slightly overestimated.
[16] https://www.ligo.caltech.edu/news/ligo20220617
[17] https://www.gw-openscience.org/O3/index/

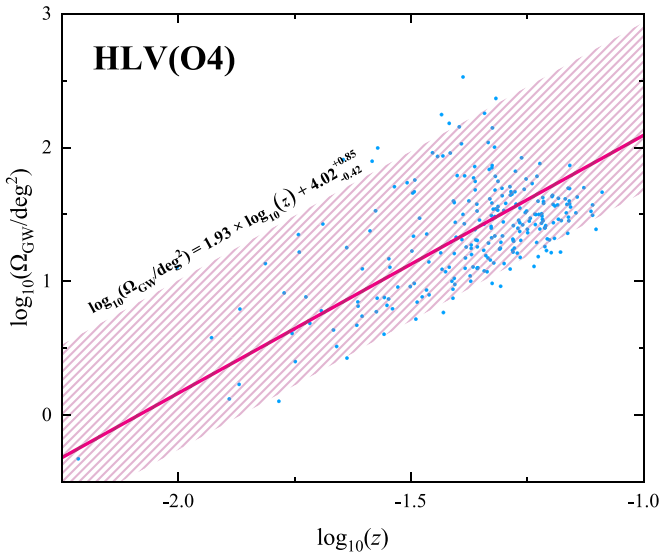

Figure 6. 90% confidence of GW sky localization vs. redshift for BNS mergers detected at the HLV (O4) era when all three GW detectors are online at the same time.

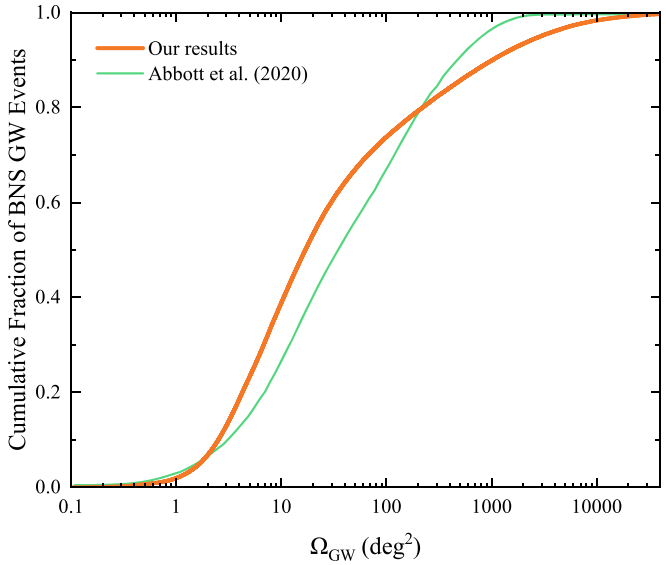

Figure 7. Cumulative fractions of BNS GW events with sky localization areas during O4 smaller than the abscissa value. Our simulation results are marked by the thick orange line, while the model distribution from Abbott et al. (2020a) is shown with a thin green line.

corresponding era have reached the design sensitivity and work normally" as the optimal situation. During the 2.5th-generation detector network, the best case is that A+, AdV+, and KAGRA+ all work normally, which we abbreviate as "PlusNetwork." LIGO Voyager is separately discussed. Furthermore, "ET&CE" represents the best case of the third-generation era.

We need to localize the BNS through GW signals for EM follow-ups. As we need to calculate a large number of simulated signals, we use the Fisher information matrix (FIM; Cutler & Flanagan 1994) to approximate the localization area estimated by the more computationally expensive Bayesian method (Thrane & Talbot 2019). The FIM is based on linear signal approximation (LSA; Cutler & Flanagan 1994) and uses a Gaussian distribution to approximate the posterior distribution of the parameters. This assumption requires the signal to have a sufficiently high S/N, so we only calculate the GW localization for the signal whose network S/N meets the detection threshold. The FIM of the detector network is a linear summation of the FIM of the individual detector in that network

$$\mathbf{\Gamma}_{ij} = \sum_k \langle \partial_i h | \partial_j h \rangle_k, \tag{6}$$

where the bracket means the inner product

$$\langle a|b\rangle = 4\Re \int_{f_{\min}}^{f_{\max}} \frac{\tilde{a}(f)\tilde{b}^*(f)}{S_n(f)}\, df, \tag{7}$$

where k is the index of the detector in that network, and $\partial_i h$ or $\partial_j h$ refers to the partial differentiation of the detector-frame signal in the frequency domain with respect to a certain parameter. In our FIM calculation, the parameters are chosen from the detector-frame chirp mass $\mathcal{M}$, the symmetric mass ratio η, the luminosity distance D_L, the coalescence time t_c, the coalescence phase ϕ_c, the inclination angle l, the polarization angle ψ, the R.A. θ, the decl. ϕ, and the tidal deformation parameters $\tilde{\Lambda}$ and $\delta\tilde{\Lambda}$. Note that, for the third-generation detector network, we also take the Earth's rotation into account (Liu & Shao 2022). In order to reduce the matrix singularity issue, we do not take partial differentiation of the tidal parameters for the cases before the third-generation.

For high-S/N signals, the inverse of the FIM is less or equal to the covariance matrix of parameters, the so-called "Cramer–Rao lower bound"

$$\mathrm{cov}(i,j) \geqslant (\mathbf{\Gamma}^{-1})_{ij}; \tag{8}$$

for a specific parameter, we can use the square root of the corresponding diagonal element in the inverse of the FIM as the bias. In our case, we care about $\Delta\cos\theta$ and $\Delta\phi$. Then we can derive the sky localization area (Barack & Cutler 2004)

$$\Omega_{GW} = 2\pi\sqrt{\langle(\Delta\cos\theta\Delta\phi)^2\rangle - \langle\Delta\cos\theta\Delta\phi\rangle^2}; \tag{9}$$

we consider a 90% confidence of this area hereafter.

4.2. GW Detections and EM Follow-ups in the Second-generation Era

4.2.1. GW Detection Rate, Detectable Distance, and Sky Localization

We consider the exact duty cycle shown in Table 5, and the simulated GW detection results of O3 and O4 are summarized in Table 6. We check that the GW detection rate in O3 should be $\sim 2.4^{+3.6}_{-1.8}$ yr^{-1}, which is consistent with the observations of LVC (Abbott et al. 2020a, 2021c). The median detectable luminosity distance is $\sim$110 Mpc, nearly approximate to the observed distance of GW190425 (Abbott et al. 2020b). In the HLV (O4) era, we predict that one can detect $\sim$11 yr^{-1} BNS GW events with the median detectable distance at $z \sim 0.040$ and the horizon at $z_{\max} \sim 0.084$.

We simulate the sky localization area (Ω_{GW}) for detectable BNS GW events when two or three detectors are online simultaneously during O4. As the localization for GW mainly relies on the time delay between different detectors, one second-generation GW detector cannot localize GW signals. We find that the relationship between the sky localization and redshift for BNS mergers detected in O4 with the H1, L1, and VIRGO network can be well explained by a log-linear trend (Figure 6), while the

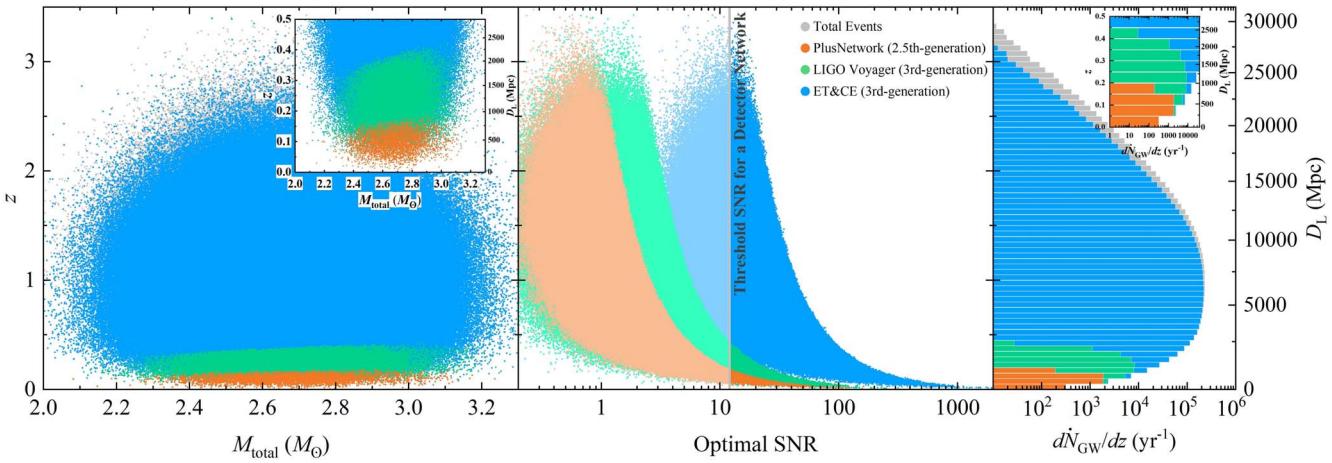

Figure 8. Detectability of BNS mergers by various detector networks in different GW detection eras. The left panels show the signals that can be detected by different detectors and detector networks. The orange, green, and blue dots are the GW signals detectable at the PlusNetwork, LIGO Voyager, and ET&CE network eras, respectively. The gray dots in the background represent the undetectable signals. The small panels in the upper right corner are enlarged images of the low-redshift area. The middle panels show the distributions of all simulated signals on the "optimal S/N–redshift" plane, with the detection thresholds of the detector network (i.e., S/N = 12; light gray line). To the right of the thresholds are the GW signals that can be detected. The right panels show the distributions of the BNS detection rates with the redshift, and the insets are zoom-in pictures of the low-redshift region.

log-linear relationships with only two GW detectors network are not obvious due to their limited detections. In Figure 7, the median sky localization area is expected to be $\sim$10 deg^2 for detectable BNS GW events. We also collected the cumulative fraction of the sky localization from Abbott et al. (2020a). Comparing with our simulation, they considered the operation of K1 in O4 and used the BAYESTAR (Singer & Price 2016) code to perform sky localization for BNS GW events. A duty cycle of 70% for each detector uncorrelated with the other detectors, which is slightly different from our simulations, was adopted by Abbott et al. (2020a). However, our simulation result for the sky localization in O4 is nearly consistent with that shown in Abbott et al. (2020a).

4.2.2. EM Detectability in O4

Based on the BNS GW detection results during O4, we now estimate the EM detection rates of detectable BNS GW events for ZTF, SiTian, Mephisto, WFST, and LSST. For serendipitous observations, the event would appear in an arbitrary position of the celestial sphere due to the lack of ToO alerts. For the GW-triggered ToO observations, the survey project would just need to cover the sky localization of GW events in search of their associated EM counterparts. Thus, one can replace $\Omega_{\rm sph}$ with $\Omega_{\rm GW}$ in Equation (4) to estimate the EM detection rate for the ToO observations, i.e.,

$$\dot{N}_{\rm EM} \approx \frac{\dot{N}_{\rm BNS}}{n_{\rm sim}} \cdot \frac{\Omega_{\rm cov}}{\Omega_{\rm sph}} \times \sum_{i=1}^{n_{\rm GW}} \sum_{j} \frac{\Omega_{\rm FoV} P_{{\rm duty},j} \min(t_{{\rm cad},ij},\ \Delta t_{ij})}{\max(\Omega_{\rm FoV},\ \Omega_{{\rm GW},j})(n_{{\rm exp},ij} t_{{\rm exp},ij} + t_{\rm oth})}, \quad (10)$$

where $j = \{\rm HL,\ HV,\ LV,\ HLV\}$ and $n_{\rm GW}$ represents the number of detectable BNS GW events. Here, we adopt $t_{\rm exp} = 300$ s to make GW-triggered follow-up observations. Thus, the cadence time $t_{\rm cad}$ for each event is related to $t_{\rm exp}$ and $\Omega_{\rm GW}$ for each event. The judgment condition for the detection of the kilonova and/or afterglow by a follow-up search after GW triggers is required to be *two different exposure filters have at least two detection epochs*.

As SiTian will not operate during O4, we only show our simulated detection rates for ZTF, Mephisto, WFST, and LSST at this era. Based on the technical information of the survey projects listed in Table 2, our simulation results show that ZTF/SiTian/Mephisto/WFST/LSST can detect $\sim$5/4/3/3 kilonovae ($\sim$1/1/1/1 afterglows) in O4, respectively. $\sim$5% kilonovae and $\sim$90% afterglows after GW triggers are expected to be associated with the detection of sGRBs.

4.3. GW Detections and EM Follow-ups in the 2.5th- and Third-generation Eras

4.3.1. GW Detection Rate, Detectable Distance, and Sky Localization

We summarize all our simulated GW detection results of the 2.5th- and third-generation eras in Table 6. The total mass, S/N, and redshift for the detectable GW signals in different eras are shown in Figure 8. For the 2.5th-generation GW detector network, the optimal detection rate is $\sim$210 yr^{-1}. The GW detection distance would be doubled compared with the detection distance in O4, i.e., the horizon can reach $z_{\rm max} \sim 0.2$. For the LIGO Voyager in the third-generation era, the optimal detection rate can be increased to $\sim$1800 yr^{-1} and the detection distance would be twice compared with that in the last era, i.e., a horizon of $z_{\rm max} \sim 0.4$. However, these numbers are much smaller than those for the newly designed third-generation detectors. For the ET&CE network, the optimal detection rate would be $\sim 2.4 \times 10^5$ yr^{-1}, which would account for $\sim$91% of the total BNS GW events in the universe. The events detected by ET&CE are mainly dominated by BNS mergers at $z \sim 1$, which is near the most probable redshift where BNS mergers occurred in the universe. The most remote detectable events by ET&CE would be at $z_{\rm max} \sim 3.8$. Except for the ET&CE era, the median distance of detectable GW events is always set to half of the horizon in each GW era.

In Figure 9, the relationships between the 90% credible area of GW sky localization and the redshift for BNS mergers detected at the PlusNetwork, LIGO Voyager, and ET&CE eras can be represented by log-linear trends, similar to that of the

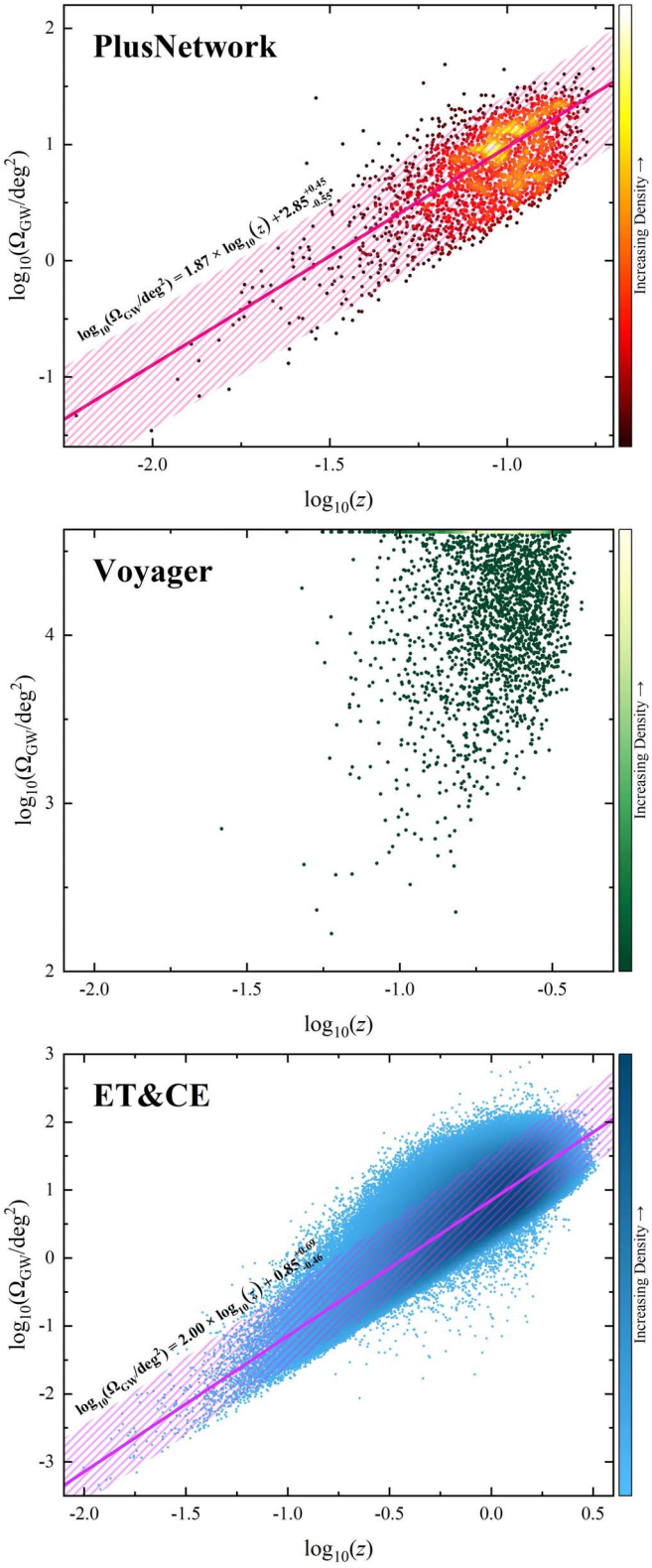

Figure 9. 90% confidence of GW sky localization vs. redshift for BNS mergers detected at the PlusNetwork (top panel), LIGO Voyager (middle panel), and ET&CE (bottom panel) eras, respectively. The density (see the color bar of each panel) for the points is calculated via the kernel density estimation. The solid line and shaded region in each panel represent the median of the GW sky localization and 90% interval, respectively.

second-generation network. The fitting results of these log-linear trends are listed in Table 6. In the PlusNetwork era, most of detectable BNS mergers will be localized to $\lesssim 10\,\mathrm{deg}^2$. The network comprising one ET detector and two CE detectors can have a more remarkable capability to observe and localize BNS GW events. For BNS mergers occurring at $z \lesssim 0.2$, the GW sky localizations constrained in the ET&CE era will be about 2 orders of magnitude lower than those constrained in the PlusNetwork era. The median localization for BNS mergers at $z \sim 0.5$ ($z \sim 1$) is shown to be $\sim 1\,\mathrm{deg}^2$ ($\sim 10\,\mathrm{deg}^2$). In these regimes, the present and future wide-FoV survey projects will be able to cover the sky localizations given by GW detections in a few pointings and achieve deep detection depths with relatively short exposure integration times. As the current GW operation plan during the LIGO Voyager era only includes two GW detectors, we find that the sky localizations will span from a few hundred square degrees to tens of thousands of square degrees. Thus, EM follow-ups might be very difficult if there are no more GW detectors to join the campaign at the LIGO Voyager era.

4.3.2. EM Detectability

The BNS GW detectabilities for the networks of 2.5th- and third-generation GW detectors have been studied in detail in Section 4.3.1. Based on these results, we now discuss the EM detection probabilities and optimistic EM detection rates for GW-triggered ToO observations.

As the luminosity distributions in different bands are consistent, we only show g-band luminosity distributions for the EM signals of detectable GW events at different GW eras in Figure 10. For the future GW eras of PlusNetwork, LIGO Voyager, and ET&CE, the critical magnitudes for the detection of EM emissions from all BNS GW events would be $\sim$23.5 mag, $\sim$25 mag, and $\gtrsim$26 mag, respectively. Present and foreseeable-future survey projects can hardly find all EM signals of BNS GW events detected during the ET&CE era. Comparing with the results of adjacent GW eras, one can see that there appears little difference in the number of detectable kilonovae if adopting the detection depth as the critical magnitude of earlier GW eras. However, one can find much more remote sGRBs and afterglows in later GW eras. As the search limiting magnitude increases, the amount of detectable kilonovae would increase exponentially. There is also an exponential increase with a slower rising slope for the amount of afterglows. At the critical magnitude of each era, $\sim$80% BNS GW events can observe clear kilonova signals, while afterglows would account for the other $\sim$20% BNS GW events. Most of the detectable kilonova-dominated BNS GW events would be not accompanied by observations of sGRBs. Kilonova events associated with sGRBs like the observations of GW170817/GRB170817A/AT2017gfo would be scarce.

Based on the GW detections in different eras, we then estimate the optimistic EM detection rates for specific survey projects listed in Table 2. Under ideal operation conditions in the PlusNetwork and ET&CE eras, due to the precise sky localizations of GW events, these survey projects will be able to cover the sky localizations given by GW detections in a few pointings. Thus, we define $\Omega_{\rm cov}/\Omega_{\rm GW} \sim 1$ in Equation (10) to estimate the EM detection rates. We note that, although the current plan in the LIGO Voyager era shows relatively poor sky localization for GW events, we still estimate the EM detection rate of this era by defining $\Omega_{\rm cov}/\Omega_{\rm GW} \sim 1$ under the assumption that more GW detectors joining the campaign might significantly improve the sky localizations. The optimistic detection rates of EM signals at different GW eras

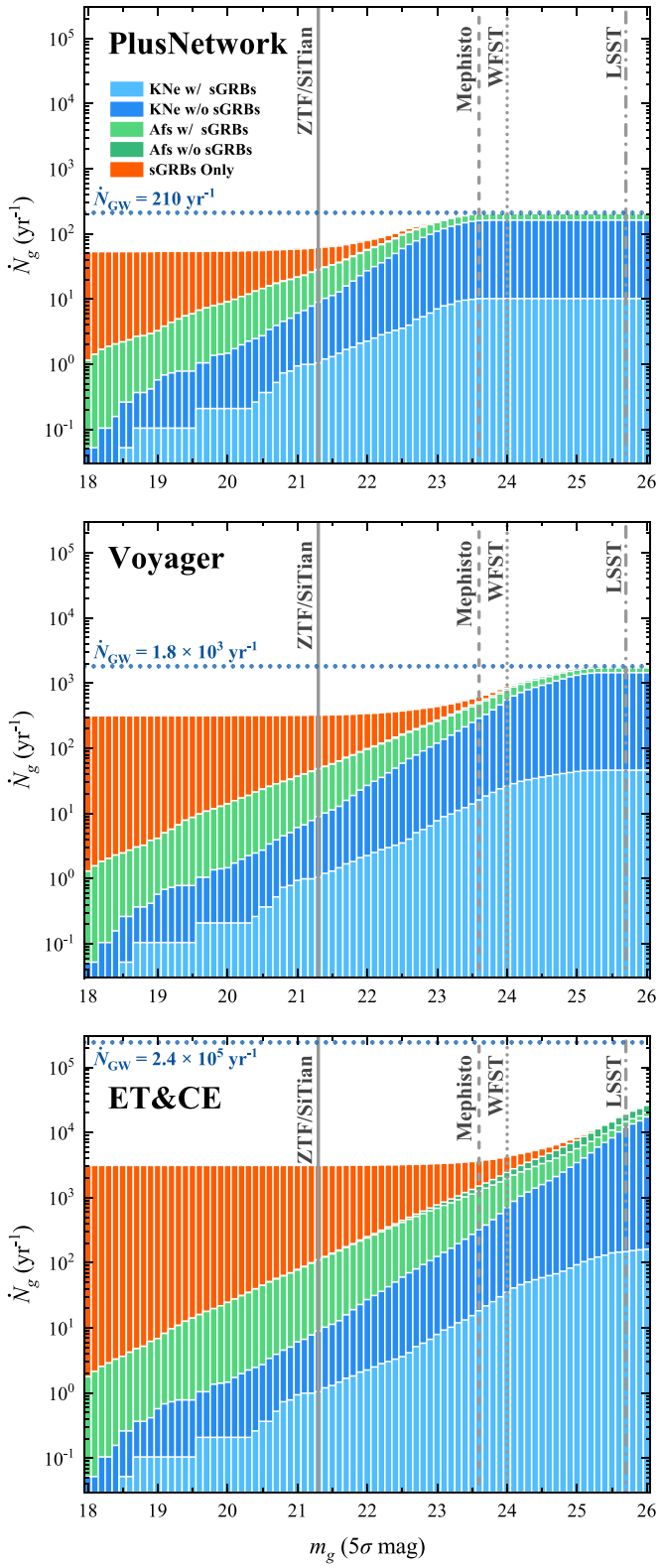

Figure 10. g-band luminosity functions for the delectable samples of kilonovae w/sGRBs (light blue histograms), kilonovae w/o sGRBs, (dark blue histograms), afterglows w/sGRBs (light green histograms), afterglow w/o sGRBs (dark green histograms), and only sGRBs (orange histograms) as functions of the g-band 5σ limiting magnitude during three GW detection eras, i.e., the PlusNetwork, LIGO Voyager, and ET&CE eras. The gray solid, dashed, dotted, and dashed–dotted lines, respectively, represent the r-band 5σ limiting magnitude of ZTF/SiTian, Mephisto, WFST, and LSST, with a 300 s exposure time. The dashed blue lines shows the GW detection rates in each GW era. The bin width of the histograms is set to $\Delta = 0.1$ mag.

for specific survey projects are displayed in Figure 11 and labeled in Table 7. By comparing the limiting magnitudes of specific survey projects and the critical magnitudes in the different GW eras (Figure 10), we find that these wide-field surveys (ZTF, SiTian, Mephisto, and WFST) are unlikely to detect a larger number of kilonovae despite the upgraded GW detectors improving the BNS detection rates. Optimistically, ZTF/SiTian/Mephisto/WFST can detect ∼5/5/150/120 kilonovae per year at the 2.5th- and third-generation eras, while ∼100/300/1200 yr^{-1} kilonovae per year can be discovered by LSST during the PlusNetwork/LIGO Voyager/ET&CE eras, respectively. At later GW eras, ToO observations of BNS GW events can always discover more afterglows, almost all of which are associated with sGRBs. However, we find a special case in which LSST follow-up in the ET&CE era will detect as much as ∼75% of detectable afterglows, which will be largely orphans unaccompanied by an sGRB.

5. Conclusions and Discussion

In this paper, based on our model proposed in the companion paper (Paper I), we have presented the serendipitous search detectability of time-domain surveys for BNS EM signals, the detectability of GWs for different generations of GW detectors, as well as joint-search GW signals and optical EM counterparts.[18]

Serendipitous observations—We have systematically made simulations of optimal search strategy for searching for kilonova and afterglow emissions from BNS mergers by serendipitous observations. For our selected survey projects, which include ZTF/Mephisto/WFST/LSST, we have found that a one-day cadence serendipitous search with an exposure time of ∼30 s can always achieve near-maximum detection rates for kilonovae and afterglows. The optimal detection rates of kilonova-dominated (afterglow-dominated) events are ∼0.3/0.6/1/20 yr^{-1} (∼50/60/100/800 yr^{-1}), respectively, for the survey projects of ZTF/Mephisto/WFST/LSST. As for the survey array of the SiTian project, we have shown that when the array fully operates it will discover more kilonova events if a longer exposure time is adopted. The detection rate of kilonova (afterglow) events could even reach ∼7(2 × 10^3) yr^{-1} by SiTian. The population properties and fading rates of the detectable kilonovae and afterglows have been studied in detail. Our results have shown that afterglows are easier to detect than kilonovae by these survey projects. These afterglows detected by optically serendipitous observations should always be associated with sGRBs. However, present survey projects have not detected as many afterglows as we have predicted. One reason may be that only part of BNS GW events could generate relativistic jets and power bright afterglows (e.g., Sarin et al. 2022). Genuine weather fluctuations and operational issues of optical telescopes might contribute to the deficit of detection. Actual survey observations cannot always achieve the prospective detection depth and cadence, which could be another cause of the lack of enough afterglow observations. Furthermore, a relatively longer cadence interval for traditional survey projects has been adopted to discover ordinary supernovae or tidal-disruption events. These cadence intervals are significantly larger than the timescales during which the

[18] GW and EM detectability in the decihertz GW band could be found in Liu et al. (2022) and Kang et al. (2022).

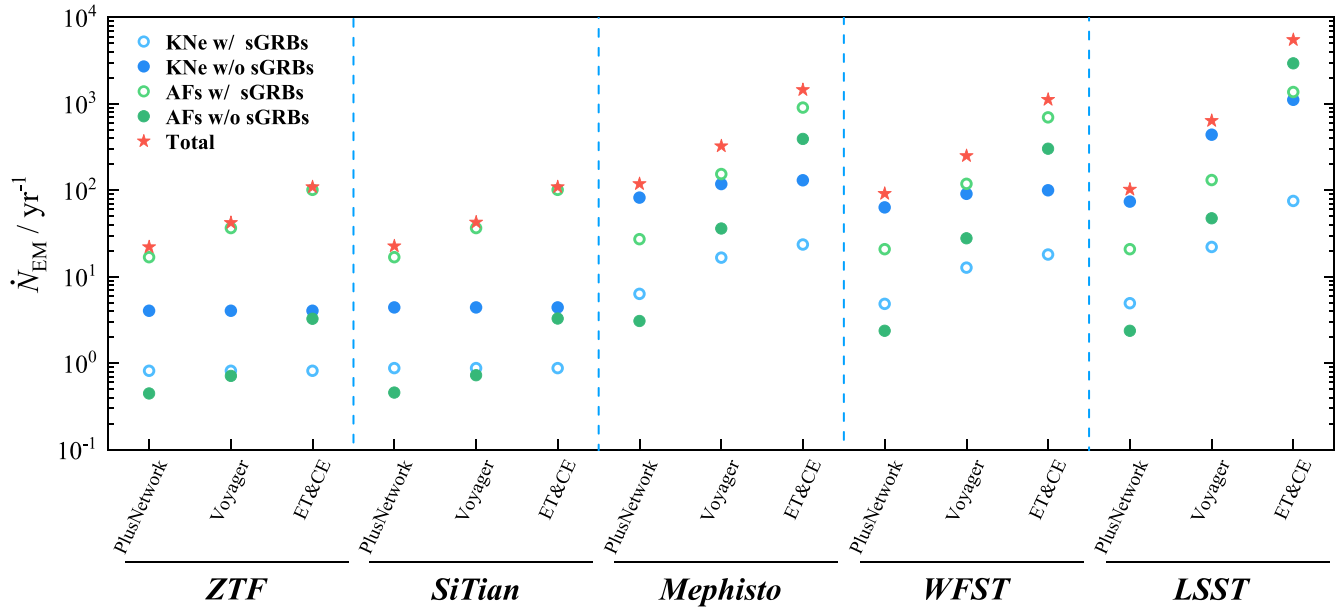

Figure 11. *g*-band optimistic detection rates of kilonovae w/sGRBs (light blue circles), kilonovae w/o sGRBs (dark blue circles), afterglows w/sGRBs (light green circles), afterglows w/o sGRBs (dark blue circles), and total EM signals (red stars) for specific survey projects (including ZTF, SiTian, Mephisto, WFST, and LSST) in the PlusNetwork, Voyager, and ET&CE eras.

Table 7
g-band Optimistic EM Detection Rates in Each GW Era

Sample	Era	ZTF	SiTian	Mephisto	WFST	LSST
KNe w/sGRBs	PlusNetwork	0.8	0.9	6.3	4.9	4.9
	Voyager	0.8	0.9	16.6	12.8	22.1
	ET&CE	0.8	0.9	23.6	18.1	75.4
KNe w/o sGRBs	PlusNetwork	4.0	4.4	82.4	63.4	74.0
	Voyager	4.0	4.4	118	90.9	438
	ET&CE	4.0	4.4	130	100	1.11×10^3
AFs w/sGRBs	PlusNetwork	16.8	16.8	27.1	20.9	20.9
	Voyager	36.6	36.6	154	118	131
	ET&CE	101	101	905	696	1.37×10^3
AFs w/o sGRBs	PlusNetwork	0.4	0.5	3.1	2.4	2.4
	Voyager	0.7	0.7	36.2	27.9	47.4
	ET&CE	3.3	3.3	392	302	2.93×10^3
Total EM Signals	PlusNetwork	22.1	22.6	119	91.5	102
	Voyager	42.2	42.7	325	250	639
	ET&CE	109	110	1.45×10^3	1.12×10^3	5.49×10^3

Note. The values represent the simulated BNS merger detection rates (in unit of yr^{-1}) in different GW eras.

brightness of the afterglow is above the limiting magnitude (as shown in Table 3), so afterglow events could be easily missed. Recently, thanks to the improved cadence, ZTF has discovered seven independent optically discovered GRB afterglows without any detection of an associated kilonova (Andreoni et al. 2021). Among these detected afterglows, at least one event was inferred to be associated with an sGRB. This ZTF observation may support our afterglow simulations but also shows a possible low efficiency in detecting afterglows. Thus, such selection criteria may miss most kilonova events. Conversely, the low efficiency of afterglow observations also indicates the difficulty of searching for kilonova signals by serendipitous observations. Andreoni et al. (2021, 2022) intended to select kilonova and afterglow candidates from a survey database by considering recorded sources with rates rising faster than 1 mag day^{-1} and rates fading faster than 0.3 mag day^{-1}. When $m_{\rm limit} \lesssim 22$ mag, our detailed studies on the population properties of detectable kilonovae and afterglows reveal that their detected fading rates peak at $\sim$0–0.1 mag day^{-1} and $\sim$1.3 mag day^{-1}, respectively.

GW detections and ToO follow-ups during O4—By applying the duty cycle of O3 to simulate the GW observations during O4, we predict that one can detect $\sim$11 yr^{-1} BNS GW events with a median detectable distance of $z \sim 0.040$ and a horizon of $z_{\rm max} \sim 0.084$. The median sky localization area is expected to be $\sim$10 deg^2 for detectable BNS GW events in O4. Based on the public alert

distributions in O3, Petrov et al. (2022) suggested that the threshold S/N for the detection of BNSs might be lower (i.e., S/N > 9). Following their suggestions, the detection rate of BNS mergers would be higher, and the median GW sky localization area would be larger in O4 in comparison with our simulations. In this paper, we adopt their respective design sensitivities to simulate GW detections and ToO follow-ups of GW triggers as their sensitivities are dynamic and change over time. After the completion of this work, we notice that the detection sensitivities of H1, L1, V1, and K1 in upcoming O4 have been updated.[19] Based on their latest detection sensitivities, our simulations of the detection rate, detectable distance, and sky localization might be slightly better than they will really be. During O4, our simulations show that ZTF/Mephisto/WFST/LSST will detect ∼5/4/3/3 kilonovae (∼1/1/1/1 afterglows) per year, respectively. Most of these detectable afterglows are expected to be associated with sGRBs, while only $\lesssim$5% kilonovae can simultaneously detect their associated sGRBs after GW triggers.

GW detections and ToO follow-ups at the 2.5th- and third-generation eras—We have carried out detailed calculations of the detection capabilities of the 2.5th- and third-generation detector networks in the near future for BNS GW signals. Optimistically, we show that the GW detection rate and detection horizon for the PlusNetwork are $\sim 210\,\mathrm{yr}^{-1}$ and $z_{\max} \sim 0.2$, respectively. Most of the detectable BNS mergers will be localized at $\lesssim 10\,\mathrm{deg}^2$, which is always smaller than the FoVs of most survey projects. For the LIGO Voyager in the third-generation era, the optimal detection rate can be increased to $\sim 1800\,\mathrm{yr}^{-1}$ and the detection distance would be twice that of the last era, i.e., a horizon of $z_{\max} \sim 0.4$. The ET&CE network is expected to detect all BNS merger events in the entire universe, with detection rates of $\sim 2.4 \times 10^5\,\mathrm{yr}^{-1}$. As the sensitivity of GW detectors increases, BNS events at high redshifts gradually dominate the detected events. At this era, the detection rate is mainly dominated by BNS mergers at $z \sim 1$. The median localization for BNS mergers at $z \sim 0.5$ ($z \sim 1$) is shown to be $\sim 1\,\mathrm{deg}^2$ ($\sim 10\,\mathrm{deg}^2$). In the PlusNetwork and LIGO Voyager eras, the critical magnitudes for the detection of EM emissions from all BNS GW events would be ∼23.5 mag and ∼25 mag, respectively. At the critical magnitude of each era, in ∼80% of BNS GW events we can observe clear kilonova signals, while afterglows would account for the other ∼20% BNS GW events. ZTF/SiTian/Mephisto/WFST can optimistically detect ∼5/5/150/120 kilonovae per year at the 2.5th- and third-generation eras, while $\sim 100/300/1200\,\mathrm{yr}^{-1}$ kilonovae per year can be discovered by LSST during the PlusNetwork/LIGO Voyager/ET&CE eras, respectively. At later GW eras, ToO observations of BNS GW events can always discover more afterglows, almost all of which are associated with sGRBs. Present and foreseeable-future survey projects can hardly find all EM signals of BNS GW events detected during the ET&CE era. By assuming a single-Gaussian structured jet model (e.g., Zhang & Mészáros 2002), we have shown that GW170817-like events, which can be simultaneously observed as an off-axis sGRB and a clear kilonova, may be scarce. In order to explain the sGRB signal of GW170817/GRB170817A, a two-Gaussian structured jet model may be required (Tan & Yu 2020). Future multimessenger detection rates of sGRBs, kilonovae, and afterglows can be used for constraining the jet structure.

In this paper, we adopt an AT2017gfo-like model as our standard kilonova model to calculate the kilonova detectability of serendipitous and GW-triggered ToO observations. However, many theoretical works in the literature (e.g., Kasen et al. 2013, 2017; Darbha & Kasen 2020; Kawaguchi et al. 2020, 2021; Korobkin et al. 2021; Wollaeger et al. 2021) show that BNS kilonovae should be diverse, depending on the mass ratio of the binary and the nature of the merger remnant. The possible energy injection from the merger remnant, e.g., due to the spin-down of a post-merger magnetar (Yu et al. 2013, 2018; Metzger & Piro 2014; Ai et al. 2018; Li et al. 2018; Ren et al. 2019)[20] or fallback accretion onto the post-merger BH (Rosswog 2007; Ma et al. 2018) could significantly increase the brightness of a kilonova. The diversity of kilonovae and potential energy injection may affect the final detection rate of kilonovae, which will be studied in future work.

We thank the anonymous referees for constructive comments. We thank Xue-Feng Wu and Jiming Yu for valuable comments. The work of J.P.Z. is partially supported by the National Science Foundation of China under grant No. 11721303 and the National Basic Research Program of China under grant No. 2014CB845800. Y.P.Y. is supported by National Natural Science Foundation of China grant No. 12003028, the National Key Research and Development Program of China (2022SKA0130101), and the China Manned Spaced Project (CMS-CSST-2021-B11). Z.J.C. is supported by the National Natural Science Foundation of China (No. 11690023). H.G. is supported by the National Natural Science Foundation of China under grant No. 11690024, 12021003, 11633001. Y.W.Y. is supported by the National Natural Science Foundation of China under grant No. 11822302, 11833003. L.S. is supported by the National Natural Science Foundation of China under grant No. 11975027, and the Max Planck Partner Group Program funded by the Max Planck Society.

Software: `POSSIS` (Bulla 2019; Coughlin et al. 2020a); Matlab, https://www.mathworks.com; Python, https://www.python.org; LALSuite (LIGO Scientific Collaboration 2018).

Appendix
Amplitude Spectral Density

The ASD sensitivity curves of GW detectors used in our calculations are presented in Figure 12. For O3, we adopt GW190814's sensitivity curves[21] as the O3 sensitivity. The detector sensitivities during the HLV (O4), PlusNework, and LIGO Voyager eras are adopted from the public data.[22,23] The sensitivity curves of ET and CE used in this paper come from the official websites.[24,25]

[19] https://observing.docs.ligo.org/plan/

[20] The dissipation of wind from a remnant magnetar (Zhang 2013) or interaction between the relativistic magnetar-driven ejecta and the circumstellar medium (Gao et al. 2013a; Liu et al. 2020) may also produce additional optical emission.

[21] https://dcc.ligo.org/P2000183/public

[22] https://dcc.ligo.org/LIGO-P1200087-v42/public

[23] https://dcc.ligo.org/LIGO-T1500293/public

[24] http://www.et-gw.eu/index.php/etsensitivities

[25] https://dcc.cosmicexplorer.org/cgi-bin/DocDB/ShowDocument?docid=T2000017

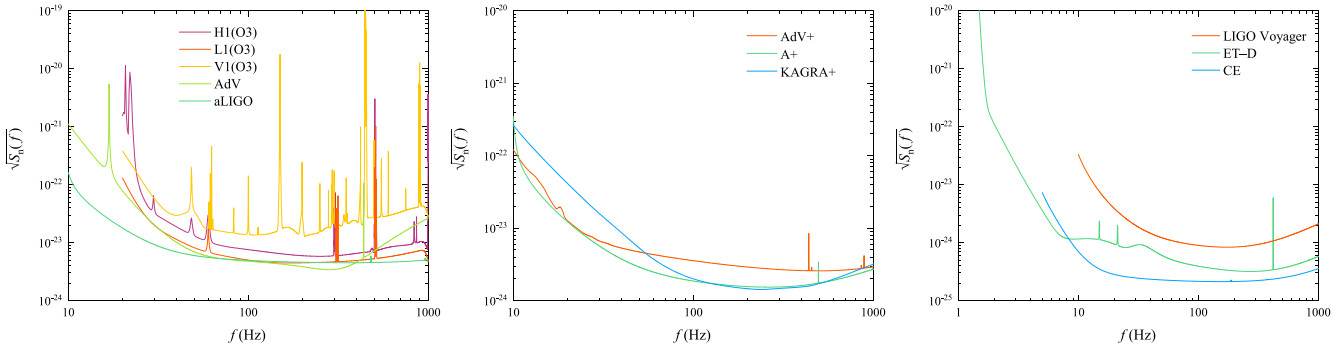

Figure 12. Left panel: design sensitivity curves of second-generation GW detectors and O3 sensitivity curves. Middle panel: design sensitivity curves of 2.5th-generation GW detectors. Right panel: design sensitivity curves of third-generation GW detectors.

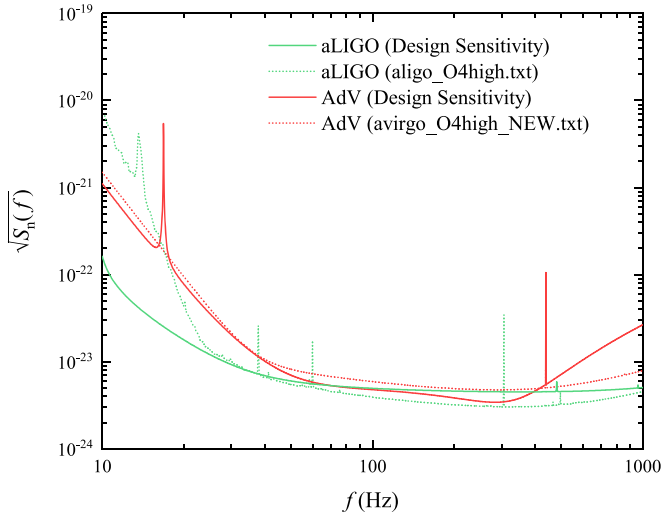

Figure 13. Design sensitivity curves (sold lines) and latest O4 sensitivity curves (dashed lines) of Advanced LIGO (red lines) and Advanced Virgo (green lines).

For second-generation detectors, we also compare their design sensitivity curves to the latest sensitivity curves released on 2022 April 6[26] in Figure 13.

ORCID iDs

Jin-Ping Zhu https://orcid.org/0000-0002-9195-4904
Shichao Wu https://orcid.org/0000-0002-9188-5435
Yuan-Pei Yang https://orcid.org/0000-0001-6374-8313
Chang Liu https://orcid.org/0000-0001-7649-6792
Bing Zhang https://orcid.org/0000-0002-9725-2524
Hao-Ran Song https://orcid.org/0000-0002-7348-4304
He Gao https://orcid.org/0000-0002-3100-6558
Zhoujian Cao https://orcid.org/0000-0002-1932-7295
Yun-Wei Yu https://orcid.org/0000-0002-1067-1911
Yacheng Kang https://orcid.org/0000-0001-7402-4927
Lijing Shao https://orcid.org/0000-0002-1334-8853

References

Abbott, B. P., Abbott, R., Abbott, T. D., et al. 2017a, PhRvL, 119, 161101
Abbott, B. P., Abbott, R., Abbott, T. D., et al. 2017b, ApJL, 848, L13
Abbott, B. P., Abbott, R., Abbott, T. D., et al. 2017c, ApJL, 848, L12
Abbott, B. P., Abbott, R., Abbott, T. D., et al. 2019, PhRvX, 9, 011001
Abbott, B. P., Abbott, R., Abbott, T. D., et al. 2020a, LRR, 23, 3

[26] https://dcc.ligo.org/LIGO-T2000012-v2/public

Abbott, B. P., Abbott, R., Abbott, T. D., et al. 2020b, ApJL, 892, L3
Abbott, R., Abbott, T. D., Abraham, S., et al. 2021a, ApJL, 915, L5
Abbott, R., Abbott, T. D., Abraham, S., et al. 2021b, ApJL, 913, L7
Abbott, R., Abbott, T. D., Abraham, S., et al. 2021c, PhRvX, 11, 021053
Acernese, F., Agathos, M., Agatsuma, K., et al. 2015, CQGra, 32, 024001
Adhikari, R. X., Arai, K., Brooks, A. F., et al. 2020, CQGra, 37, 165003
Ai, S., Gao, H., Dai, Z.-G., et al. 2018, ApJ, 860, 57
Alexander, K. D., Berger, E., Fong, W., et al. 2017, ApJL, 848, L21
Almualla, M., Anand, S., Coughlin, M. W., et al. 2021, MNRAS, 504, 2822
Andreoni, I., Ackley, K., Cooke, J., et al. 2017, PASA, 34, e069
Andreoni, I., Coughlin, M. W., Almualla, M., et al. 2022, ApJS, 258, 5
Andreoni, I., Coughlin, M. W., Kool, E. C., et al. 2021, ApJ, 918, 63
Arcavi, I., Hosseinzadeh, G., Howell, D. A., et al. 2017, Natur, 551, 64
Ascenzi, S., Coughlin, M. W., Dietrich, T., et al. 2019, MNRAS, 486, 672
Aso, Y., Michimura, Y., Somiya, K., et al. 2013, PhRvD, 88, 043007
Barack, L., & Cutler, C. 2004, PhRvD, 69, 082005
Bellm, E. C., Kulkarni, S. R., Graham, M. J., et al. 2019, PASP, 131, 018002
Berger, E., Fong, W., & Chornock, R. 2013, ApJL, 774, L23
Broekgaarden, F. S., Berger, E., Neijssel, C. J., et al. 2021, MNRAS, 508, 5028
Bulla, M. 2019, MNRAS, 489, 5037
Chase, E. A., O'Connor, B., Fryer, C. L., et al. 2022, ApJ, 927, 163
Cheng, K. S., & Wang, J.-M. 1999, ApJ, 521, 502
Chornock, R., Berger, E., Kasen, D., et al. 2017, ApJL, 848, L19
Coughlin, M., Dietrich, T., Kawaguchi, K., et al. 2017, ApJ, 849, 12
Coughlin, M. W., Antier, S., Dietrich, T., et al. 2020a, NatCo, 11, 4129
Coughlin, M. W., Dietrich, T., Antier, S., et al. 2020b, MNRAS, 497, 1181
Coulter, D. A., Foley, R. J., Kilpatrick, C. D., et al. 2017, Sci, 358, 1556
Covino, S., Wiersema, K., Fan, Y. Z., et al. 2017, NatAs, 1, 791
Cowperthwaite, P. S., Berger, E., Villar, V. A., et al. 2017, ApJL, 848, L17
Cowperthwaite, P. S., Villar, V. A., Scolnic, D. M., & Berger, E. 2019, ApJ, 874, 88
Cutler, C., & Flanagan, E. E. 1994, PhRvD, 49, 2658
Darbha, S., & Kasen, D. 2020, ApJ, 897, 150
D'Avanzo, P., Campana, S., Salafia, O. S., et al. 2018, A&A, 613, L1
D'Avanzo, P., Salvaterra, R., Bernardini, M. G., et al. 2014, MNRAS, 442, 2342
Díaz, M. C., Macri, L. M., Garcia Lambas, D., et al. 2017, ApJL, 848, L29
Dietrich, T., Samajdar, A., Khan, S., et al. 2019, PhRvD, 100, 044003
Dobie, D., Kaplan, D. L., Murphy, T., et al. 2018, ApJL, 858, L15
Drout, M. R., Piro, A. L., Shappee, B. J., et al. 2017, Sci, 358, 1570
Drozda, P., Belczynski, K., O'Shaughnessy, R., Bulik, T., & Fryer, C. L. 2022, A&A, 667, A126
Eichler, D., Livio, M., Piran, T., & Schramm, D. N. 1989, Natur, 340, 126
Evans, P. A., Cenko, S. B., Kennea, J. A., et al. 2017, Sci, 358, 1565
Fan, Y.-Z., Yu, Y.-W., Xu, D., et al. 2013, ApJL, 779, L25
Fong, W., Berger, E., Margutti, R., & Zauderer, B. A. 2015, ApJ, 815, 102
Fong, W., Laskar, T., Rastinejad, J., et al. 2021, ApJ, 906, 127
Fong, W.-f., Nugent, A. E., Dong, Y., et al. 2022, ApJ, 940, 56
Frostig, D., Biscoveanu, S., Mo, G., et al. 2022, ApJ, 926, 152
Gao, H., Ding, X., Wu, X.-F., Dai, Z.-G., & Zhang, B. 2015, ApJ, 807, 163
Gao, H., Ding, X., Wu, X.-F., Zhang, B., & Dai, Z.-G. 2013a, ApJ, 771, 86
Gao, H., Lei, W.-H., Zou, Y.-C., Wu, X.-F., & Zhang, B. 2013b, NewAR, 57, 141
Gao, H., Zhang, B., & Lü, H.-J. 2016, PhRvD, 93, 044065
Gao, H., Zhang, B., Lü, H.-J., & Li, Y. 2017, ApJ, 837, 50
Gehrels, N., Chincarini, G., Giommi, P., et al. 2004, ApJ, 611, 1005

Ghirlanda, G., Salafia, O. S., Paragi, Z., et al. 2019, Sci, 363, 968
Goldstein, A., Veres, P., Burns, E., et al. 2017, ApJL, 848, L14
Gompertz, B. P., Levan, A. J., Tanvir, N. R., et al. 2018, ApJ, 860, 62
Haggard, D., Nynka, M., Ruan, J. J., et al. 2017, ApJL, 848, L25
Hallinan, G., Corsi, A., Mooley, K. P., et al. 2017, Sci, 358, 1579
Hao, J.-M., & Yuan, Y.-F. 2013, A&A, 558, A22
Harry, G. M. & LIGO Scientific Collaboration 2010, CQGra, 27, 084006
Hu, L., Wu, X., Andreoni, I., et al. 2017, SciBu, 62, 1433
Hu, R.-C., Zhu, J.-P., Qin, Y., et al. 2022, ApJ, 928, 163
Jin, Z.-P., Covino, S., Liao, N.-H., et al. 2020, NatAs, 4, 77
Jin, Z.-P., Hotokezaka, K., Li, X., et al. 2016, NatCo, 7, 12898
Jin, Z.-P., Li, X., Cano, Z., et al. 2015, ApJL, 811, L22
Kagra Collaboration, Akutsu, T., Ando, M., et al. 2019, NatAs, 3, 35
Kang, Y., Liu, C., & Shao, L. 2022, MNRAS, 515, 739
Kasen, D., Badnell, N. R., & Barnes, J. 2013, ApJ, 774, 25
Kasen, D., Metzger, B., Barnes, J., Quataert, E., & Ramirez-Ruiz, E. 2017, Natur, 551, 80
Kasliwal, M. M., Anand, S., Ahumada, T., et al. 2020, ApJ, 905, 145
Kasliwal, M. M., Nakar, E., Singer, L. P., et al. 2017, Sci, 358, 1559
Kawaguchi, K., Fujibayashi, S., Shibata, M., Tanaka, M., & Wanajo, S. 2021, ApJ, 913, 100
Kawaguchi, K., Shibata, M., & Tanaka, M. 2020, ApJ, 889, 171
Kilpatrick, C. D., Foley, R. J., Kasen, D., et al. 2017, Sci, 358, 1583
Kiziltan, B., Kottas, A., De Yoreo, M., & Thorsett, S. E. 2013, ApJ, 778, 66
Korobkin, O., Wollaeger, R. T., Fryer, C. L., et al. 2021, ApJ, 910, 116
Lattimer, J. M. 2012, ARNPS, 62, 485
Lazzati, D., Perna, R., Morsony, B. J., et al. 2018, PhRvL, 120, 241103
Lei, L., Li, J., Wu, J., Jiang, S., & Chen, B. 2021, AR&T, 18, L18
Li, L.-X., & Paczyński, B. 1998, ApJL, 507, L59
Li, S.-Z., Liu, L.-D., Yu, Y.-W., & Zhang, B. 2018, ApJL, 861, L12
Lien, A., Sakamoto, T., Gehrels, N., et al. 2014, ApJ, 783, 24
LIGO Scientific Collaboration 2018, LIGO Algorithm Library—LALSuite, Free Software (GPL), https://git.ligo.org/lscsoft/lalsuite
LIGO Scientific Collaboration, Aasi, J., Abbott, B. P., et al. 2015, CQGra, 32, 074001
Lipunov, V. M., Gorbovskoy, E., Kornilov, V. G., et al. 2017, ApJL, 850, L1
Liu, C., Kang, Y., & Shao, L. 2022, ApJ, 934, 84
Liu, C., & Shao, L. 2022, ApJ, 926, 158
Liu, J., Soria, R., Wu, X.-F., Wu, H., & Shang, Z. 2021, AnABC, 93, 20200628
Liu, L.-D., Gao, H., & Zhang, B. 2020, ApJ, 890, 102
LSST Science Collaboration, Abell, P. A., Allison, J., et al. 2009, arXiv:0912.0201
Lyman, J. D., Lamb, G. P., Levan, A. J., et al. 2018, NatAs, 2, 751
Ma, S.-B., Lei, W.-H., Gao, H., et al. 2018, ApJL, 852, L5
Ma, S.-B., Xie, W., Liao, B., et al. 2021, ApJ, 911, 97
Maggiore, M., Van Den Broeck, C., Bartolo, N., et al. 2020, JCAP, 2020, 050
Mandel, I., & Broekgaarden, F. S. 2022, LRR, 25, 1
Margutti, R., Berger, E., Fong, W., et al. 2017, ApJL, 848, L20
Masci, F. J., Laher, R. R., Rusholme, B., et al. 2019, PASP, 131, 018003
McCully, C., Hiramatsu, D., Howell, D. A., et al. 2017, ApJL, 848, L32
McKernan, B., Ford, K. E. S., & O'Shaughnessy, R. 2020, MNRAS, 498, 4088
Meegan, C., Lichti, G., Bhat, P. N., et al. 2009, ApJ, 702, 791
Mészáros, P., & Rees, M. J. 1993, ApJ, 405, 278
Mészáros, P., & Rees, M. J. 1997, ApJ, 476, 232
Metzger, B. D., & Berger, E. 2012, ApJ, 746, 48
Metzger, B. D., Martínez-Pinedo, G., Darbha, S., et al. 2010, MNRAS, 406, 2650
Metzger, B. D., & Piro, A. L. 2014, MNRAS, 439, 3916
Michimura, Y., Komori, K., Enomoto, Y., et al. 2020, PhRvD, 102, 022008
Miller, J., Barsotti, L., Vitale, S., et al. 2015, PhRvD, 91, 062005
Mohite, S. R., Rajkumar, P., Anand, S., et al. 2022, ApJ, 925, 58
Nakar, E., Gal-Yam, A., & Fox, D. B. 2006, ApJ, 650, 281
Narayan, R., Paczynski, B., & Piran, T. 1992, ApJL, 395, L83
Nicholl, M., Berger, E., Kasen, D., et al. 2017, ApJL, 848, L18
Nugent, A. E., Fong, W.-f., Dong, Y., et al. 2022, ApJ, 940, 57
O'Connor, B., Troja, E., Dichiara, S., et al. 2022, MNRAS, 515, 4890
Paczynski, B. 1986, ApJL, 308, L43
Paczynski, B. 1991, AcA, 41, 257
Paczynski, B., & Rhoads, J. E. 1993, ApJL, 418, L5
Perna, R., Lazzati, D., & Cantiello, M. 2021, ApJL, 906, L7
Petrov, P., Singer, L. P., Coughlin, M. W., et al. 2022, ApJ, 924, 54
Pian, E., D'Avanzo, P., Benetti, S., et al. 2017, Natur, 551, 67
Piro, L., Troja, E., Zhang, B., et al. 2019, MNRAS, 483, 1912
Planck Collaboration, Ade, P. A. R., Aghanim, N., et al. 2016, A&A, 594, A13
Punturo, M., Abernathy, M., Acernese, F., et al. 2010a, CQGra, 27, 194002
Punturo, M., Abernathy, M., Acernese, F., et al. 2010b, CQGra, 27, 084007
Rastinejad, J. C., Gompertz, B. P., Levan, A. J., et al. 2022, Natur, 612, 223
Rees, M. J., & Meszaros, P. 1992, MNRAS, 258, 41
Reitze, D., Adhikari, R. X., Ballmer, S., et al. 2019, BAAS, 51, 35
Ren, J., Lin, D.-B., Zhang, L.-L., et al. 2019, ApJ, 885, 60
Rossi, A., Stratta, G., Maiorano, E., et al. 2020, MNRAS, 493, 3379
Rosswog, S. 2007, MNRAS, 376, L48
Rosswog, S., Feindt, U., Korobkin, O., et al. 2017, CQGra, 34, 104001
Sagués Carracedo, A., Bulla, M., Feindt, U., & Goobar, A. 2021, MNRAS, 504, 1294
Sari, R., Piran, T., & Narayan, R. 1998, ApJL, 497, L17
Sarin, N., Lasky, P. D., Vivanco, F. H., et al. 2022, PhRvD, 105, 083004
Savchenko, V., Ferrigno, C., Kuulkers, E., et al. 2017, ApJL, 848, L15
Scolnic, D., Kessler, R., Brout, D., et al. 2018, ApJL, 852, L3
Setzer, C. N., Biswas, R., Peiris, H. V., et al. 2019, MNRAS, 485, 4260
Shappee, B. J., Simon, J. D., Drout, M. R., et al. 2017, Sci, 358, 1574
Shi, D.-D., Zheng, X.-Z., Zhao, H.-B., et al. 2018, AcASn, 59, 1
Singer, L. P., & Price, L. R. 2016, PhRvD, 93, 024013
Singh, K. P., Tandon, S. N., Agrawal, P. C., et al. 2014, Proc. SPIE, 9144, 91441S
Smartt, S. J., Chen, T. W., Jerkstrand, A., et al. 2017, Natur, 551, 75
Soares-Santos, M., Holz, D. E., Annis, J., et al. 2017, ApJL, 848, L16
Song, H.-R., Ai, S.-K., Wang, M.-H., et al. 2019, ApJL, 881, L40
Sun, H., Zhang, B., & Li, Z. 2015, ApJ, 812, 33
Tan, W.-W., & Yu, Y.-W. 2020, ApJ, 902, 83
Tanvir, N. R., Levan, A. J., Fruchter, A. S., et al. 2013, Natur, 500, 547
Tanvir, N. R., Levan, A. J., González-Fernández, C., et al. 2017, ApJL, 848, L27
Thrane, E., & Talbot, C. 2019, PASA, 36, e010
Troja, E., Fryer, C. L., O'Connor, B., et al. 2022, Natur, 612, 228
Troja, E., Piro, L., Ryan, G., et al. 2018, MNRAS, 478, L18
Troja, E., Piro, L., van Eerten, H., et al. 2017, Natur, 551, 71
Troja, E., van Eerten, H., Zhang, B., et al. 2020, MNRAS, 498, 5643
Typel, S., Röpke, G., Klähn, T., Blaschke, D., & Wolter, H. H. 2010, PhRvC, 81, 015803
Utsumi, Y., Tanaka, M., Tominaga, N., et al. 2017, PASJ, 69, 101
Valenti, S., Sand, D. J., Yang, S., et al. 2017, ApJL, 848, L24
Villar, V. A., Guillochon, J., Berger, E., et al. 2017, ApJL, 851, L21
Virgili, F. J., Zhang, B., O'Brien, P., & Troja, E. 2011, ApJ, 727, 109
Vitale, S., & Evans, M. 2017, PhRvD, 95, 064052
Vitale, S., & Whittle, C. 2018, PhRvD, 98, 024029
Wanderman, D., & Piran, T. 2015, MNRAS, 448, 3026
Wollaeger, R. T., Fryer, C. L., Chase, E. A., et al. 2021, ApJ, 918, 10
Wu, G.-L., Yu, Y.-W., & Zhu, J.-P. 2021, A&A, 654, A124
Xie, X., Zrake, J., & MacFadyen, A. 2018, ApJ, 863, 58
Yang, B., Jin, Z.-P., Li, X., et al. 2015, NatCo, 6, 7323
Yang, F., Wang, W., Wei, X., et al. 2022a, RAA, 22, 055005
Yang, J., Ai, S., Zhang, B.-B., et al. 2022b, Natur, 612, 232
Yu, J., Song, H., Ai, S., et al. 2021, ApJ, 916, 54
Yu, Y.-W., Liu, L.-D., & Dai, Z.-G. 2018, ApJ, 861, 114
Yu, Y.-W., Zhang, B., & Gao, H. 2013, ApJL, 776, L40
Yuan, Y., Lü, H.-J., Yuan, H.-Y., et al. 2021, ApJ, 912, 14
Zappa, F., Bernuzzi, S., Pannarale, F., Mapelli, M., & Giacobbo, N. 2019, PhRvL, 123, 041102
Zevin, M., Nugent, A. E., Adhikari, S., et al. 2022, ApJL, 940, L18
Zhang, B. 2013, ApJL, 763, L22
Zhang, B. 2018, The Physics of Gamma-Ray Bursts (Cambridge: Cambridge Univ. Press)
Zhang, B., & Mészáros, P. 2002, ApJ, 571, 876
Zhang, B. B., Zhang, B., Sun, H., et al. 2018, NatCo, 9, 447
Zhang, D.-L., Li, X.-Q., Xiong, S.-L., et al. 2019, NIMPA, 921, 8
Zhu, J.-P., Wang, K., & Zhang, B. 2021a, ApJL, 917, L28
Zhu, J.-P., Wang, K., Zhang, B., et al. 2021b, ApJL, 911, L19
Zhu, J.-P., Wang, X. I., Sun, H., et al. 2022a, ApJL, 936, L10
Zhu, J.-P., Wu, S., Qin, Y., et al. 2022b, ApJ, 928, 167
Zhu, J.-P., Wu, S., Yang, Y.-P., et al. 2021c, ApJ, 921, 156
Zhu, J.-P., Wu, S., Yang, Y.-P., et al. 2021d, ApJ, 917, 24
Zhu, J.-P., Yang, Y.-P., Liu, L.-D., et al. 2020, ApJ, 897, 20
Zhu, J.-P., Yang, Y.-P., Zhang, B., Gao, H., & Yu, Y.-W. 2022c, ApJ, 938, 147
Zhu, J.-P., Zhang, B., Yu, Y.-W., & Gao, H. 2021e, ApJL, 906, L11